Siina Pamilo

# Spatio-temporal segregation of brain circuitries activated during movie viewing

**Low Temperature Laboratory, Brain Research Unit**
**Department of Biomedical Engineering and Computational Science**

Thesis submitted for examination for the degree of Master of Science in Technology.
Espoo March 11th, 2011

**Thesis supervisor:**

Prof. Mikko Sams

**Thesis instructors:**

D.Sc. (Tech.) Sanna Malinen

Academy Professor Riitta Hari

Aalto University
School of Science

AALTO UNIVERSITY
SCHOOL OF SCIENCE

ABSTRACT OF THE
MASTER'S THESIS

Author: Siina Pamilo

Title: Spatio-temporal segregation of brain circuitries activated during movie viewing

Date: March 11th, 2011 Language: English Number of pages:9+50

Low Temperature Laboratory, Brain Research Unit
Department of Biomedical Engineering and Computational Science
Professorship: Cognitive technology Code: S-114

Supervisor: Prof. Mikko Sams

Instructors: D.Sc. (Tech.) Sanna Malinen, Academy Professor Riitta Hari

So called resting state networks (RSNs), *i.e.* functionally connected brain areas that are active both during rest and task conditions, are receiving growing attention in modern brain research. The first observed RSN was the motor network. Since then, several different cortical networks have been identified. In this thesis the focus was on the sensorimotor, dorsal attention and default-mode networks.

Independent component analysis (ICA) was used to segregate the three cortical networks from fMRI data collected from 15 subjects who were watching a 15 minutes long film ("At land" by Maya Deren). ICA was performed at three different dimensionalities and the effect of increasing the number of component estimates was examined. The functional connectivity between brain areas occupied by the three networks was examined also with seed-based correlation. The stimulus-related brain areas were indentified with intersubject correlation (ISC) analysis and the ICs were sorted according to the spatial overlap with the ISC map. The time courses of the most stimulus related ICs were compared with events in the movie.

At a low dimensionality of ICA (25), the ICs representing the sensorimotor and dorsal attention networks included brain areas that do not belong to the networks. With an intermediate number of components (40) the additional areas were separated from the networks. This dimensionality was apparently closest to the correct one. When the dimensionality was further increased (70), the networks split into subcomponents. Although the spatial splitting was physiologically sensible, the time courses of the ICs got distorted at a too high dimensionality. The results of this work contribute to understanding how the number of components affects the group-ICA results and how the correct number of ICs could be empirically controlled in group-fMRI data.

Keywords: fMRI, ICA, seed-based correlation, ISC, RSN, naturalistic stimulation, human brain, movie

AALTO-YLIOPISTO
PERUSTIETEIDEN KORKEAKOULU

DIPLOMITYÖN
TIIVISTELMÄ

Tekijä: Siina Pamilo

Työn nimi: Elokuvan katselun aktivoimien aivoverkostojen ajallispaikallinen erottelu

Päivämäärä: 11.3.2011 Kieli: Englanti Sivumäärä:9+50

Kylmälaboratorio, Aivotutkimusyksikkö
Lääketieteellisen tekniikan ja laskennallisen tieteen laitos
Professuuri: Kognitiivinen teknologia Koodi: S-114

Valvoja: Prof. Mikko Sams

Ohjaajat: TkT Sanna Malinen, Akatemiaprofessori Riitta Hari

Niin levon kuin tehtävän suorituksen aikana aktiiviset, toisiinsa toiminnallisesti kytkeytyneet aivoalueet, eli nk. lepoverkostot, ovat yksi nykyaikaisen aivotutkimuksen erityisistä mielenkiinnon kohteista. Ensimmäiseksi havaittiin motorinen verkosto, minkä jälkeen on löydetty monia muita aivoverkostoja. Tässä diplomityössä tutkittiin sensorimotorista ja dorsaalista tarkkaavaisuus verkostoa sekä nk. default mode -verkostoa.

Nämä kolme aivoverkostoa erotettiin 15 minuutin pituisen elokuvan ("At Land", Maya Deren) katselun aikana 15 koehenkilöltä kerätystä fMRI-datasta riippumattomien komponenttien analyysillä (ICA). Estimoitujen riippumattomien komponenttien (IC) lukumäärän vaikutusta ryhmä-ICAn tuloksiin tarkasteltiin kolmella eri komponenttimäärällä. ICAlla löydettyjen aivoverkostojen toiminnallinen yhteys todettiin myös lähdekorrelaatiomenetelmällä. Korrelaatioanalyysin (ISC) avulla paikannettiin ärsykkeeseen liittyvät aivoalueet ja ICt järjestettiin ISC-kartan avulla. Näin pystyttiin tunnistamaan ärsykkeeseen reagoivat komponentit, joiden aikasarjoja verrattiin elokuvan tapahtumiin.

Pienellä komponenttimäärällä (25) sensorimotorista ja tarkkaavaisuusverkostoa vastaavat komponentit sisälsivät myös näihin verkostoihin kuulumattomia aivoalueita. Kun komponenttimäärää kasvatettiin (40), ylimääräiset alueet erottuivat omiksi verkostoikseen, josta voitiin olettaa, että tämä komponenttimäärä oli lähellä oikeaa. Suurella komponenttimäärällä (70) aivoverkostot jakaantuivat pienempiin osiin. Vaikka spatiaalinen jakaantuminen oli fysiologisesti mielekästä, komponenttien aikasarjat vääristyivät liian suurella komponenttimäärällä. Tämän työn tulokset auttavat ymmärtämään, miten riippumattomien komponenttien lukumäärä vaikuttaa ryhmä-ICAn tuloksiin. Tuloksia voidaan soveltaa oikean komponenttimäärän kokeellisessa etsimisessä ryhmä-fMRI datasta.

Avainsanat: fMRI, ICA, lähdekorrelaatio, korrelaatioanalyysi, lepoverkosto, luonnonmukainen ärsyke, aivot, elokuva

# Preface

This work was done in collaboration with the aivoAALTO project at the Brain Research Unit of the Low Temperature Laboratory (LTL) and at the Advanced Magnetic Imaging Centre (AMI) of the Aalto University School of Science. I would like to thank my instructors Sanna Malinen and Riitta Hari for their patient guidance and expert advice. I am also grateful to my supervisor Mikko Sams for allowing me to choose this interesting topic for my thesis. My sincere thanks goes to Yevhen Hlushchuk, Pia Tikka and Marita Kattelus for fMRI data collection. Special thanks goes to Yevhen for his help in pre-processing of the data and to Ville Renvall for his constructive comments related to MRI physics. Finally, I owe my deepest gratitude to my family and friends for support and encouragement.

Otaniemi, March 11th, 2011

Siina Pamilo

# Contents

# Symbols and abbreviations

## Symbols

| | |
|---|---|
| $\vec{B_0}$ | Magnetic field strength |
| $\vec{J}$ | Angular momentum |
| $\vec{M}$ | Magnetization |
| $\vec{\mu}$ | Dipole magnetic moment |
| $\gamma$ | Gyromagnetic ratio |
| $\hbar$ | Reduced Planck's constant |
| $\omega_0$ | Larmor frequency |
| $\omega_{RF}$ | Angular frequency of radio-frequency radiation |
| $s$ | Spin quantum number |
| $m_s$ | Magnetic quantum number |
| $E_\uparrow$ | Energy of spins aligned with the external magnetic field |
| $E_\downarrow$ | Energy of spins aligned anti-parallel to the external magnetic field |
| $E_{RF}$ | Energy of the radio-frequency radiation |
| T1 | Time constant for longitudial relaxation |
| T2 | Time constant for transversal relaxation |
| $T2^*$ | Time constant for enhanced transversal relaxation |
| $T2'$ | Time constant for transversal relaxation caused by field inhomogeneities |
| $\beta_i$ | $i$th parameter weight |
| $g_i$ | $i$th covariate |
| $\epsilon$ | Error term |
| $\mathbf{X}$ | Measured data |
| $\widetilde{\mathbf{X}}$ | Whitened data |
| $\mathbf{A}$ | Mixing matrix |
| $\widetilde{\mathbf{A}}$ | Whitened mixing matrix |
| $\mathbf{W}$ | Inverse of the mixing matrix |
| $\mathbf{S}$ | Independent components |
| $\mathbf{E}$ | Orthogonal matrix of eigenvectors |
| $\mathbf{D}$ | Diagonal matrix of eigenvalues |
| $\Theta_k$ | Model parameter of $k$th order |
| $\lambda_i$ | $i$th eigenvalue |
| $\mathbf{F_i}$ | Reducing matrix for subject $i$ |
| $\mathbf{G}$ | Reducing matrix for the concatenated data set |
| $\hat{\mathbf{A}}$ | Mixing matrix for group data |
| $\hat{\mathbf{S}}$ | Group independent components |

## Operators

| | |
|---|---|
| $E\{\cdot\}$ | Expectation |
| $\mathcal{F}\{\cdot\}$ | Fourier transform |
| $H(\cdot)$ | Entropy |
| $I(\cdot)$ | Mutual information |
| $L(\cdot)$ | Maximum log-likelihood |
| $G(\cdot)$ | Penalty term for model complexity |
| $\sum_i$ | Sum over index $i$ |
| $\prod_i$ | Product over index $i$ |

## Abbreviations

| | |
|---|---|
| BOLD | Blood oxygen level dependent (signal) |
| CBF | Cerebral blood flow |
| $CMRO_2$ | Cerebral metabolic rate of oxygen consumption |
| DAQ | Data aquisition |
| DMN | Default-mode network |
| EPI | Echo planar imaging |
| FA | Flip angle |
| FEF | Frontal eye field |
| FFG | Fusiform gyrus |
| FID | Free induction decay |
| fMRI | Functional magnetic resonance imaging |
| FOV | Field of view |
| FWE | Family-wise error |
| GLM | General linear model |
| HDR | Haemodynamic response |
| HRF | Haemodynammic response function |
| IC | Independent component |
| ICA | Independent component analysis |
| IPS | Intraparietal sulcus |
| ISC | Inter-subject correlation |
| MDL | Minimum description length |
| MI | Primary motor cortex |
| MNI | Montreal Neurological Institute |
| MR | Magnetic resonance |
| MRI | Magnetic resonance imaging |
| MT | Middle temporal |
| NMR | Nuclear magnetic resonance |
| PCA | Principal component analysis |
| PCC | Posterior cingulate cortex |
| PD | Proton density |
| RF | Radio frequency |
| ROI | Region of interest |
| RSN | Resting-state network |
| SI | Primary somatosensory cortex |
| SII | Secondary somatosensory cortex |
| SMA | Supplementary motor area |
| SNR | Signal-to-noise ratio |
| SPM | Statistical parametric mapping |
| TE | Echo time |
| TR | Repetition time |

# 1 Introduction

In modern brain research, the interest has grown to study brain networks, typically called resting state networks (RSNs). The networks consist of functionally connected brain areas that are active during rest and whose temporal behaviours can be modulated by external stimulation and cognitive load (1). Because the functional and anatomical connections have evolved and developed under natural conditions, real-life-like circumstances appear optimal for revealing the functional organisation of the brain. This is why many recent studies have started to use naturalistic stimulation, such as movies (2–7).

Functional resonance imaging (fMRI) is a brain imaging technique sensitive to haemodynamic changes related to brain activation. The analysis of fMRI data collected during naturalistic stimulation or rest benefits from data-driven approaches, such as independent component analysis (ICA) or seed-based correlation. These methods reveal functional connectivity without any *a priori* knowledge of the activation time course. ICA can reveal hidden independent factors from multivariate data. In fMRI, ICA can separate brain networks that are spatially independent of each other, for example the visual and auditory areas. In seed-based correlation, a "seed point" is selected and the signals from other parts of the brain are correlated with the signal from this seed point to reveal brain areas, whose temporal activations are similar and can therefore be considered to be functionally connected.

The aim of this work is to study three brain networks, *i.e.* the dorsal attention network, the sensorimotor network, and the default-mode network (DMN), that are segregated from the fMRI data collected from 15 subjects who watched a short film. Both ICA and seed-based correlation are used and the results of these two different methods are compared.

One challenge for the application of ICA in fMRI is that the number of independent components (ICs) to be computed has to be decided. Without any *a priori* information, it is impossible to know the correct number of sources, although algorithms exist for estimating the proper number. It is known that ICs representing cortical networks split into subcomponents when the number of components is increased (8–11). In this work, ICA is performed at three different dimensionalities. The aim is to examine the splitting of the ICs and to study whether the splitting is functionally relevant.

Inter-subject correlation (ISC) analysis is a data-driven method that reveals brain regions that are activated in synchrony across subjects by examining the strength of correlation between individual time courses in corresponding spatial locations. Here, ISC is utilized to find the most stimulus-related components. The time courses of the stimulus-driven ICs are compared with events in the movie. The activations are assumed to be related to specific features, such as the movements and touch of the main character (the sensorimotor network) and salient events in the movie (the attention network). Because the activity in the DMN has been shown to diminish during task performance and external stimulation (12; 13), the DMN activity is assumed to decrease when the activity in the other networks increases.

# 2 Spontaneous BOLD fluctuations in the human brain

The brain is constantly active, also during rest. This section provides a short overview of the research that has been done on spontaneous activation fluctuations in the brain and is largely based on the review by Foxe *et al.* (1). Also the three resting-state networks, which are in focus in this work, are introduced. Functional magnetic resonance imaging, the brain imaging method used in most of the studies, is explained in more detail in Section 5.7.

Typical fMRI research has focused on stimulus-dependent blood-oxygenation-level-dependent (BOLD) signal changes in the brain. However, the brain is active also during "rest", when no external stimuli are presented. The resting brain consumes 20 per cent of the body's energy whereas performing a task increases the energy consumption to only maximally 21 per cent. Recently more attention has been paid on this baseline state of the brain. Slow fluctuations (typically under 0.1 Hz) in the BOLD signal are of special interest in this context.

Biswal *et al.* (14) discovered that spontaneous BOLD fluctuations in the left somatomotor cortex correlated with the spontaneous fluctuations in the right and medial motor cortices. Since then, this observation has been replicated in several studies (15–20). Also many other RSNs have been discovered, including visual, auditory, language, default mode, episodic memory, dorsal attention and ventral attention systems (1). Brain areas in which the spontaneous BOLD activity is correlated seem to be functionally connected. These networks continue to co-vary even during sleep, anesthesia, and task performance (1). Simultaneous recordings of spontaneous fMRI fluctuations and electrical measures of brain activity, such as electroencephalography (EEG), have shown that the spontaneous fluctuations in the BOLD signal correlate well with high-frequency neuronal activity, suggesting that the resting fluctuations are a result of neuronal activity (1).

It appears that the basic correlation structures of the spontaneous activity do not disappear during task performance but they may be modulated. The correlation between brain regions similarly activated by the task or stimulus increases during task or stimulation whereas the correlation between other regions decreases (1). Two explanations have been proposed. First, the changes in the correlation structure could be due to neural reorganization through suppression and facilitation of synaptic activity (21). Second, the correlation structure during task performance would reflect a superposition of spontaneous fluctuations and task-related activation (18). The baseline state of the brain affects task performance. Many experiments have shown that the spontaneous fluctuations explain the variability of BOLD responses and behavior between trials (1).

What is the functional role of the resting-state networks? First, if either direct or indirect anatomical connections exist between the nodes of the functional networks that can explain the synchronized activity also during rest. Second, it is possible that the spontaneous fluctuations work like a memory showing correlation between brain regions in which the activation has been modulated simultaneously during a

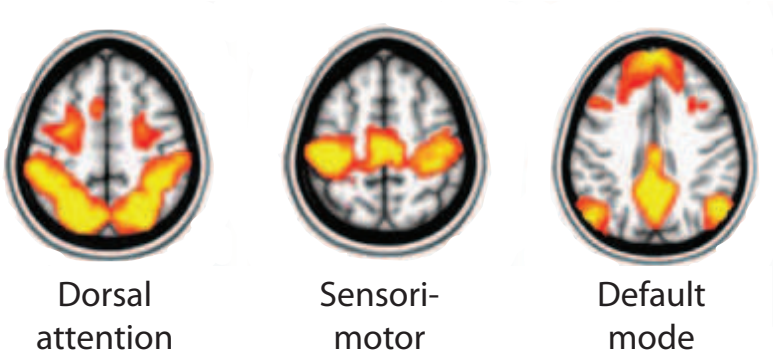


**Figure 1:** *The dorsal attention, sensorimotor and default mode networks. Figure adapted from (31) .*

task (1). Another explanation is that the spontaneous activation organizes neural activity and that the coordination is stronger between regions that commonly work together (1). The fluctuations could also serve as a dynamic prediction of the future with correlations occurring between regions that will probably be used together (1). However, no conclusive evidence exist for any of these hypotheses, and further investigation is needed.

Analysis of spontaneous BOLD data requires data-driven methods, such as seed-based correlation, hierarchical clustering, or ICA (see section 6). Independent component analysis has been widely used for analyzing both task-related and spontaneous BOLD activity within neuronal networks (8; 11; 22–29).

In this work the focus is on three brain networks: the dorsal attention, the sensorimotor, and the default-mode networks illustrated in Figure 1. The sensorimotor network covers bilaterally the primary motor and somatosensory cortices as well as the supplementary motor area (SMA). In addition some other areas have been reported to covary with these areas, such as the thalamus and cerebellum (15–20). The default mode network is distinct from the others in that its activation decreases during task performance (12; 13). It covers the posterior cingulate cortex (PCC) and precuneus, medial prefrontal cortex and bilateral inferior parietal cortex (23; 24; 30). The fluctuations in this network have been suggested to be important for the processes during rest (12). However, the exact role of this network remains unclear.

Two sensory orienting systems, the ventral and dorsal attention networks, dynamically interact and guide our attention. The dorsal attention network is involved in voluntary (top-down) processing of sensory information and links the selected sensory cues to appropriate motor responses. It includes the dorsal parietal cortex, particularly the intraparietal sulcus (IPS) and superior parietal lobule (SPL), and the junction of the precentral and superior frontal sulcus (frontal eye fields, FEFs) in each hemisphere (32). This network is activated by expectation of seeing a target in a particular location or with specific features, by the preparation of a response, or by short term memory of a visual scene (33).

The ventral attention network reorients the attention to salient stimuli in the

environment, especially when unattended. The network is lateralized to the right hemisphere and includes the right temporal-parietal junction and the right ventral frontal cortex (32; 33). It is activated when targets appear in unexpected locations or when a target appears infrequently (33). The ventral system probably detects surprising events (stimulus-driven re-orienting) and disrupts the ongoing selection in the dorsal network which then shifts the attention to the novel target (34).

# 3 Naturalistic stimulation in fMRI

In human brain imaging, the interest has recently increased towards real-life-like stimulus settings. This section covers some of the work done in this field.

Traditional fMRI experiments use rather simple block designs, and the analysis is commonly done using the general-linear-model (GLM) analysis (see section 6.2). Much of what is known about brain function by means of fMRI has been found out in this way. In the GLM approach, a hypothetical activation time course is constructed on the basis of the stimulus presentation. This time course is then compared with the measured data, and brain regions whose time courses match the modeled one in statistical sense are considered to be activated by the stimulus. Conventional fMRI experiments typically use rather simple stimuli in highly controlled conditions to reveal stimulus-dependent activations, which can be predicted and modeled. However, in real life the environment is multimodal and constantly changing. If we want to know how our brains function in such situations, the stimulus settings in brain imaging should also be as naturalistic as possible. Quite recently fMRI experiments have started to utilize more naturalistic stimulation, such as movies (2; 3; 5; 6; 35–39). Although movies are quite far from a real-life experience, they still mimic it well given the constraints of the experimental setup. On one hand, using naturalistic stimulation can reveal activity patterns that would not be found with traditional methods. On the other hand, the activations triggered by naturalistic stimulation should agree with the activations aroused by simple stimuli.

Because naturalistic stimuli often are highly unpredictable and multimodal, it may be difficult to use temporal covariates necessary for GLM analysis. The analysis of fMRI data recorded during naturalistic stimulation therefore benefits from data-driven approaches that make no assumptions on activations triggered by the stimulus. The most widely used methods are seed-based correlation, ICA, and ISC (39). Data-based analyses have shown that human brain activity can be highly reliable under naturalistic conditions (2; 3; 5–7; 35–39). The stimuli in these studies have included for example movies, audio books and music. For example, Bartels and Zeki (3) applied ICA and seed-based correlation to identify networks related to seeing, hearing and language processing. Correlations between directly connected regions increased during natural viewing while the correlation between unconnected regions decreased. In an earlier work, they used ICA to separate functionally connected brain networks from fMRI data collected during both free movie viewing and during a traditional block-design setup (2). Natural viewing activated more regions in a more distinct manner than did conventional stimuli.

# 4 Number of independent sources in fMRI data

In ICA, the number of components to be estimated has to be decided. How to determine the correct amount of independent sources in fMRI still remains an open question, although some attempts to address this issue have been recently taken. This section gives an overview of the research done concerning this problem.

Estimating too few ICA components leads to loss of information. McKeown *et al.* (29) concluded that compressing the data too much leads to loss of important information and thus it is better to estimate a large number of components. Many other studies have also concluded that a too low dimensionality causes ICA to mix various components (3; 9–11; 40). Ma *et al.* (41) detected RSNs with ICA and investigated the effect of the number of ICs on the results of ICA. They showed that a too low number of components affected the ICA results, but estimating too many components had no significant influence. An excessive reduction of the ICA dimensionality may be especially problematic when analyzing resting state fluctuations, because some of the sources are weak compared with noise (42).

On the other hand, estimating too many components causes splitting of the components (8–11). Li *et al.* (43) proposed a new method for order selection in ICA of fMRI data and showed that at too high dimensionalities the stability of the IC estimates decreases and the estimation of task related activations is degraded. Beckmann and Smith (10) examined the dependency between the number of estimated components and the accuracy of the spatial maps and time courses of the estimated ICs. On one hand, estimating too few components led to loss of information and to suboptimal signal extraction, whereas estimating too many components caused overfitting and led to arbitrary splitting of the ICs due to unconstrained estimation.

Smith *et al.* (8) investigated the splitting of RSNs, identified with ICA, using the massive BrainMap database including over 7000 functional maps collected during task conditions as well as resting state data from 36 subjects to calculate both 20-component and 70-component ICA compositions of both datasets. Similar brain networks in both datasets were found, which implies that the networks are active both in rest and during task performance. With the ICA-dimensionality of 70 the networks found in the 20-component composition split into smaller subnetworks of brain areas with slightly different function or into left- and right-sided subnetworks.

Abou-Elseoud *et al.* (9) examined the effect of increasing the model order on IC's characteristics of RSNs. Probabilistic group ICA (PICA) with ICASSO (see Section 6.5.6) was used for analyzing resting state fMRI data. At low dimensionalities, the signal sources merged into singular components, which were split into subcomponents with higher model orders. Also, some components emerged only at higher model orders whereas some did not split. The characteristics of the ICs, *i.e.* the volume and mean $z$-score, were significantly affected by the number of estimated components. The repeatability of the components decreased with increasing model order. Model orders around 70 were considered to offer a detailed and reliable evaluation of the RSNs. Increasing the dimensionality further reduced reliability, but neither the mean $z$-score nor the volume showed any statistically significant changes.

# 5 Magnetic resonance imaging

This section gives a short overview of the basic principles of magnetic resonance imaging (MRI) as well as fMRI. The introduction starts from nuclear physics and proceeds step by step to image formation and different imaging techniques. The final part of the section introduces fMRI, a MRI technique to measure brain activity. This section is based on the textbooks of Huettel *et al.* (44), Buxton (45), and Liang and Lauterbur (46).

## 5.1 A short history of MRI

Magnetic resonance imaging utilizes high magnetic fields to produce images of biological tissue. MRI is based on the phenomenon of nuclear magnetic resonance (NMR). The first NMR experiments were carried out in 1946 independently by two scientists and their research groups: Felix Bloch, working at Stanford University, and Edward Purcell from Harvard University. They found that certain nuclei placed in a magnetic field were able to absorb energy in the radiofrequency range of the electromagnetic spectrum and re-emit this energy. In 1970s, Raymond Damadian noticed that the NMR signal properties of cancerous tissue are different from that of healthy tissue. Paul Lauterbur introduced the idea of using field gradients in the magnetic field for NMR image formation and produced the first 2-D NMR image of test tubes containing water and heavy water in 1973. Peter Mansfield developed the *echo-planar-imaging* (EPI) technique for fast imaging. In the early 1980's, the first magnetic resonance imaging scanners for humans became available. Figure 2 shows the 3-T scanner used in this work located in Advanced Magnetic Imaging (AMI) Centre, Aalto University School of Science.

**Figure 2:** *The 3T-MRI scanner (AMI Centre, Aalto University School of Science) used in this work.*

## 5.2 Nuclear spins

The underlying mechanism of signal generation and detection in MRI occurs at the nuclear level. An atom consists of a nucleus, which includes protons and neutrons, and an electron shell. A fundamental property of nuclei is that they possess *spin angular momentum* $\vec{J}$, whose magnitude is given by

$$J = \hbar\sqrt{s(s+1)} \quad s = 0, \frac{1}{2}, 1, \frac{3}{2}..., \tag{1}$$

where $s$ is the *spin quantum number*, which takes either integer or half-integer values, and $\hbar$ the *reduced Planck's constant*. Nuclei with odd mass number have half-integer spin, nuclei with even mass number and even charge number have zero spin, and nuclei with even mass number and odd charge number have integral spin. In MRI, a set of nuclei of same type present in the object being imaged is called a *spin system*. For example, the hydrogen protons in the human body form a spin system. Since hydrogen ($H_1$) is the most abundant proton in the human body, it is the most commonly imaged nucleus in MRI. A hydrogen nucleus contains only one proton, so that it has a half-integer spin $s_H = \frac{1}{2}$.

Since the proton has a spin and carries a positive charge, it creates a magnetic field around it. The proton has a *magnetic dipole moment* $\vec{\mu}$, which is related to the spin angular momentum $\vec{J}$ by

$$\vec{\mu} = \gamma\vec{J}, \tag{2}$$

where $\gamma$ is a nucleus specific physical constant called the *gyromagnetic ratio*. Although the magnitude of $\vec{\mu}$ is known in any conditions, the direction of $\vec{\mu}$ is random in the absence of an external magnetic field. In an external magnetic field of strength $B_0$, applied in the $z$-direction, the $z$-component of $\mu$ can have values

$$\mu_z = \gamma m_s \hbar \quad m_s = -s, -s+1, ..., s \ , \tag{3}$$

where $m_s$ is the *magnetic quantum number*. For a hydrogen atom, the spin quantum number is equal to $\frac{1}{2}$ and thus hydrogen spin system is a spin-$\frac{1}{2}$ system. In a spin-$\frac{1}{2}$ system, the magnetic moment vector has two possible orientations: either parallel or anti-parallel to the external field.

In the external magnetic field $\vec{B_0}$, a spin experiences a torque that is equal to the rate of change of its angular momentum $\vec{J}$

$$\frac{d\vec{J}}{dt} = \vec{\mu} \times \vec{B_0}. \tag{4}$$

Because of the torque, the spin precesses about the $z$-axis with a stable angle with respect to the field. The angular frequency of this nuclear precession is

$$\omega_0 = \gamma B_0, \tag{5}$$

which is known as the *Larmor frequency*. At 3T the Larmor frequency for a $H_1$ nucleus is about 127,7 MHz.

## 5.3 Net magnetization

As noted earlier, in a spin-$\frac{1}{2}$ system, $\vec{\mu}$ can either align parallel or antiparallel to the external field. Spins in different orientations have different energy states. For the spins that are aligned parallel with the external field the energy is

$$E_{\uparrow} = -\frac{1}{2}\gamma\hbar B_0 \tag{6}$$

and for the spins aligned anti-parallel

$$E_{\downarrow} = \frac{1}{2}\gamma\hbar B_0. \tag{7}$$

Thus the energy states of the spins that are parallel to the external field are lower than those of the antiparallel spins. A spin is more likely to be in the lower energy state, so a small majority of the spins (at 3T an excess of $1 * 10^{-6}$ spins) align parallel to the field. Although the population difference of the two energy states is very small, it creates a magnetization vector $\vec{M}$ from a spin system

$$\vec{M} = \sum_{n=1}^{N_s} \vec{\mu}_n, \tag{8}$$

where $N_s$ is the number of spins. In a spin-$\frac{1}{2}$ system

$$\mu_{n,z} = \begin{cases} +\frac{1}{2}\gamma\hbar & \text{if } \mu_{n,z} \text{ is parallel to the external field} \\ -\frac{1}{2}\gamma\hbar & \text{if } \mu_{n,z} \text{ is anti-parallel to the external field} \end{cases}, \tag{9}$$

so that the magnetization vector is given by

$$\vec{M} = (\sum_{n=1}^{N_{\uparrow}} \frac{1}{2}\gamma\hbar - \sum_{n=1}^{N_{\downarrow}} \frac{1}{2}\gamma\hbar)\vec{k} = \frac{1}{2}(N_{\uparrow} - N_{\downarrow})\gamma\hbar\vec{k}. \tag{10}$$

In equilibrium, the bulk magnetization vector points along the positive direction of the $z$-axis. The transverse component of $\vec{M}$ is zero at equilibrium because the precessing magnetic moments have random phases.

## 5.4 Radio-frequency excitation

The alignment of the spins with the external field does not as such lead to any measurable signal. To generate an NMR signal, a radio-frequency (RF) pulse is sent to the system. The RF pulse is an oscillating magnetic field perpendicular to $B_0$. According to the Planck's law, electromagnetic radiation of frequency $\omega_{RF}$ carries energy

$$E_{RF} = \hbar\omega_{RF}. \tag{11}$$

To induce a transition of the spins from the lower energy state to the higher energy state, the radiation energy must be equal to the energy difference between these states

$$E_{RF} = \hbar\omega_{RF} = \Delta E = \gamma\hbar B_0. \tag{12}$$

Or more simply

$$\omega_{RF} = \omega_0. \tag{13}$$

In this *resonance condition* spins absorb the energy from the RF pulse and flip from the low energy state to the high energy state so that the longitudal component of the net magnetization $M_0$ decreases. In addition, the protons start to precess in phase, which establishes a transversal magnetization. This means that the RF pulse tippes the net magnetization vector to an angle $\theta$ with respect to the $z$-axis. The magnitude of $\theta$ is proportional to the product of the duration and amplitude of the RF pulse and is called the *flip angle* (FA). The precessing net magnetization produces a time-varying magnetic field, which induces a current in a receiving coil located in the MRI scanner. Thus, a *free induction decay* (FID) signal can be measured. As the name implies, this signal decays in time because of *spin relaxation*. After the RF pulse is turned off, the individual spins start to loose their phase coherence and thus the transversal magnetization decreases (transverse relaxation). The time constant of this decay in a homogenous field is called T2. The spins also flip back to the lower energy state, which causes the longitudal magnetization to increase. This phenomenon is known as longitudal relaxation and its time constant is called T1, which is generally longer than T2. The combined process of precession and relaxation are described by the *Bloch equations*:

$$\frac{\mathrm{d}M_x}{\mathrm{d}t} = \gamma B_0 M_y - \frac{M_x}{T_2} \tag{14}$$

$$\frac{\mathrm{d}M_y}{\mathrm{d}t} = -\gamma B_0 M_x - \frac{M_y}{T_2} \tag{15}$$

$$\frac{\mathrm{d}M_z}{\mathrm{d}t} = -\frac{M_z - M_0}{T_1}. \tag{16}$$

Due to local magnetic field inhomogeneities, the FID signal actually decays faster than could be expected from a known T2. This enhanced decay is described by a time constant called $\mathrm{T2}^*$, which plays a critical role in fMRI. It is defined as

$$\frac{1}{\mathrm{T2}^*} = \frac{1}{\mathrm{T2}} + \frac{1}{\mathrm{T2}'}, \tag{17}$$

where $\mathrm{T2}'$ reflects the dephasing effect caused by field inhomogeneity. The T1, T2, and $\mathrm{T2}^*$ values are tissue specific and are used as sources of contrast in MRI images. Figure 3 shows the effect of the RF pulse and the relaxation of the spins.

## 5.5 Gradient fields

To image a three-dimensional object, three orthogonal *gradient fields* are superimposed on the uniform external field $\vec{B_0}$. A gradient field is a spatially linearly varying

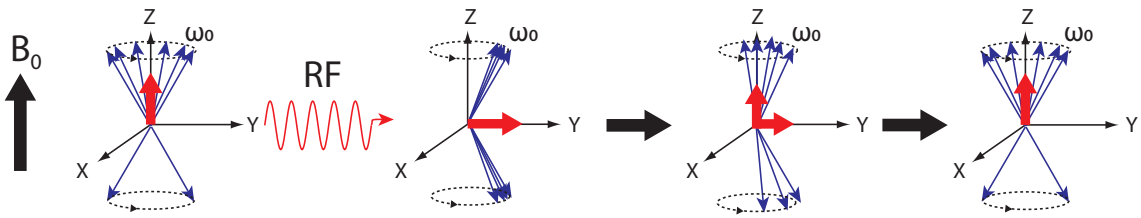


**Figure 3:** *The majority of the protons align parallel to the external magnetic field $\vec{B_0}$. The RF pulse flips some of the protons to the higher energy state (antiparallel to the external field), which causes the longitudal magnetization (red arrow) to decrease (with a 90° pulse it goes to zero, as in the figure). The protons start to precess in phase, which causes a transversal magnetization. After the RF pulse, the protons start to lose their phase coherence (transversal magnetization decays) and flip back to the lower energy state (longitudal magnetization recovers). Note that the figure is illustrative and the number of spins in the two energy states is not proportional to the true population difference.*

field produced by gradient coils in the scanner. The variations caused by the gradient fields are small compared with the main magnetic field. Since MR images are sampled in three dimensions, the basic sampling units of MRI are three-dimensional volume elements called *voxels*.

The *slice selection gradient* is applied in the same direction as the uniform magnetic field. It causes the resonance frequency of the spins to vary linearly along the $z$-axis. This gradient field is applied while an RF pulse containing only a narrow band of frequencies centered at the desired $\omega_0$ is sent. In this way it is possible to excite spins in a certain slice, *i.e.* those spins that are in resonance with the RF pulse. Slice thickness can be altered by changing the bandwidth of the RF pulse or by modifying the steepness of the gradient.

To determine a specific voxel in the slice from which the signal is coming, two additional gradients are used. The *frequency-encoding gradient* is in a typical MR-imaging sequence applied after the radio frequency pulse and it results in different precession speeds along the $x$-axis. The *phase-encoding gradient* is turned on for a short time after the RF pulse and it is perpendicular to the frequency encoding gradient. When the gradient field is applied, the protons start to precess at different frequencies. When the gradient is then turned off again, the protons go back to their former precession frequencies, but now they have different phases. The result is a mixture of signals with different frequencies and phases. The frequency and phase information are collected in a so called *k-space* (47; 48). The spatial MR image can then be reconstructed from the measured data using the *Fourier transform*.

## 5.6 Pulse sequences and image contrast

Because the signal decays in time, a new RF pulse is applied to trigger a new signal. The time between successive excitation pulses is called the *repetition time* (TR). Generally, the FID signal is not measured, but an *echo* of the original signal is

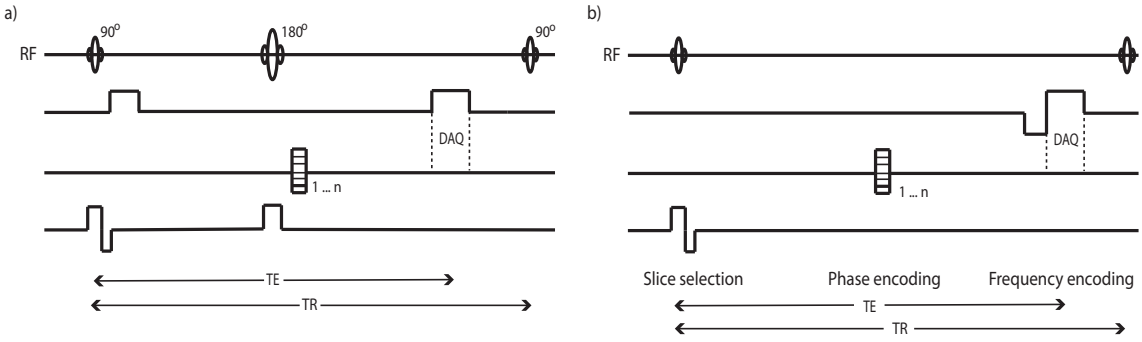


**Figure 4:** *a) A spin-echo pulse sequence and b) a gradient-echo pulse sequence. DAQ = data aquisition.*

created occurring at a time TE, the *echo time*. In a *spin-echo sequence* this is done by sending in a second RF pulse after a delay of TE/2. Commonly a 180° pulse called the *refocusing pulse* is used, because it creates the strongest echo. After the original 90° pulse, the spins start to lose their phase coherence, because they precess at slighly different rates. The spins that precess faster get ahead of the slower ones. The 180° pulse flips the spins so that the phase acquired by each spin is converted into a negative phase. Now, the faster-precessing spins are behind the slower ones. At $t$ =TE, the faster-precessing spins have caught up with the slower ones and the spins are back in phase and create an echo. A *gradient-echo sequence* uses gradient fields instead of a refocusing pulse to generate the signal echo. In this sequence a negative field gradient is turned on after the RF pulse to dephase the spins, which are then rephased by a subsequent positive gradient. Gradient-echo sequences typically use small flip angles ($< 90°$) and thus the TR can be reduced, which in turn reduces the scanning time. Figure 4 illustrates these two types of pulse sequences.

If TR is much longer than T1, the spins recover to equilibrium after each pulse and the signals after succeeding pulses are equally strong. As the TR is shortened, the signal generated by the second RF pulse becomes weaker, since the spins have not relaxed completely. Because the T1 values are tissue-specific, the spins in some

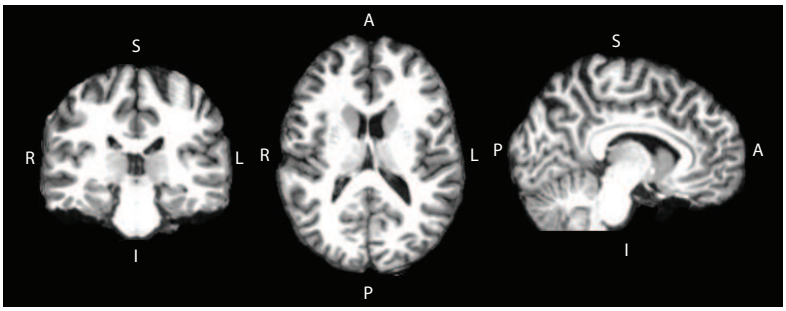


**Figure 5:** *T1-weighted skull-stripped MR image from one of the participants of this study showing coronal, axial and sagittal slices. The abbreviations refer to the orientation of the figure: right (R), left (L), superior (S), inferior (I), anterior (A), posterior (P).*

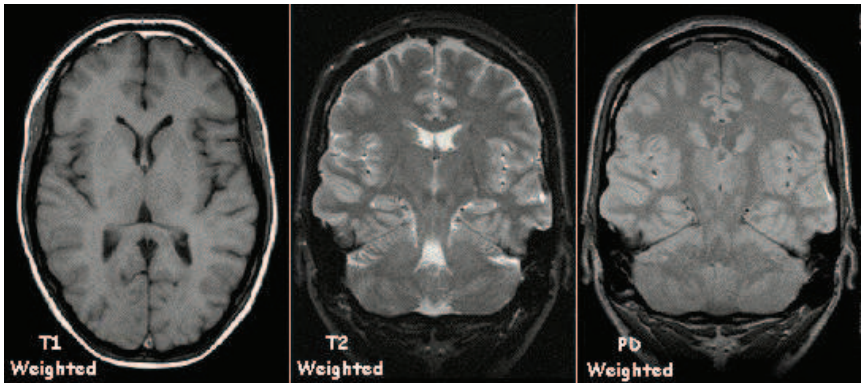


**Figure 6:** *Example of T1-, T2- and a PD-weighted images. The cerebrospinal fluid appears black in T1-weighted images and white in T2-weighted images. PD-weighted images show only little contrast between tissue types. Figure adapted from* `http://en.wikibooks.org/wiki/File:T1t2PD.jpg`.

tissues have recovered more than in others and give thus a stronger signal. This creates a contrast between different tissue types, and the resulting image is called *T1-weighted*. Fat appears bright and water dark in T1-weighted images. Figure 5 shows an example of T1-weighted MRI images in three orthogonal slice orientations: the coronal, axial and sagittal slices. Figure 6 (left) compares a T1-weighted image with images acquired with other contrast weightening.

The signal received is proportional to the net magnetization $M_0$, which in turn depends on the amount of protons in the tissue. For the tissues in the body, proton density (PD) and T1 are positively correlated. This conflicts with the T1-contrast, because a tissue with high proton density has a greater net magnetization and therefore a larger signal than a tissue with low proton density. On the other hand, long T1 tends to make the same tissue darker because there is less recovery at long T1. A *proton-density-weighted* image can be produced if the TR is long enough so that the spins have had time to relax in all tissue types. With a small flip angle the recovery is faster and the longitudal magnetization is hardly affected by the RF pulse; the sensitivity to differences in T1 is greatly reduced. Figure 6 (right) shows an example of a PD-weighted image. PD-weighted images show less contrast between tissue types than T1-weighted images.

TE is an important parameter for T2-*weighted* images. With TE $<$ T2, transversal decay is small and the T2 contrast is weak. If the TE is too long, nearly all transversal magnetization will be lost and thus there is no T2 contrast. However, with TE $\approx$ T2, the signal is strongly sensitive to the local T2, and T2 contrast can be maximized. T2-weighted images provide maximal signal from fluid-filled regions, as is seen in Figure 6 (middle).

T2$^*$-weighted images are sensitive to the relative concentration of deoxygenated haemoglobin in the blood, which changes according to the metabolic demand of active neurons. T2$^*$-contrast is best achieved with gradient echo pulse sequences with long TR and medium TE. Spin-echo sequences have reduced T2$^*$-sensitivity, because the refocusing pulse eliminates inhomogeneity effects. T2$^*$ decay forms the

basis for BOLD-contrast fMRI, described in more detail in Section 5.7.

## 5.7 Functional magnetic resonance imaging

### 5.7.1 The BOLD effect

FMRI provides information on brain physiology. The *blood oxygenation level dependent* (BOLD) effect, discovered by Ogawa and coworkers in 1990 (49), is the most widely used source of contrast in fMRI. It arises because of two distinct phenomena: the different magnetic properties of oxygenated and deoxygenated heamoglobin and changes in blood flow.

Neurons in the brain continuously consume glucose and oxygen ($O_2$), which are supplied by the *cerebral blood flow* (CBF). In the blood, oxygen is bound to *haemoglobin*. Oxygenated haemoglobin is diamagnetic whereas deoxygenated haemoglobin is paramagnetic. Therefore, changes in the relative concentration of oxygenated vs. deoxygenated haemolobin result in changes in the BOLD signal, which is stronger when less deoxygenated haemoglobin is present. In an active brain area, the cerebral metabolic rate of $O_2$ consumption ($CMRO_2$) increases and haemoglobin becomes deoxygenated. At the same time, more blood is brought to the active site. Because the blood flow increases much more than the $CMRO_2$, the amount of oxyhaemoglobin in the blood is increased and the relative concentration of deoxygenated haemoglobin is decreased, which results in a stronger MR signal.

BOLD effects are commonly measured using T2*-contrast. The presence of deoxygenated hemoglobin makes the magnetic field stronger in the red blood cells than in the surrounding plasma, which creates field inhomogeneities that shorten the T2*. In an active brain area the relative concentration of deoxygenated hemoglobin is decreased and thus the field inhomogeneities are reduced. T2* becomes longer and the signal is increased in a T2*-weighted image.

### 5.7.2 Echo planar imaging

To detect brain activity, images have to be acquired very rapidly, approximately at the same rate as the physiological changes happen. One approach to reduce the scanning time is to collect data corresponding to more than one phase-encoding step from each excitation. Figure 7 shows the most popular sequence suited for fast

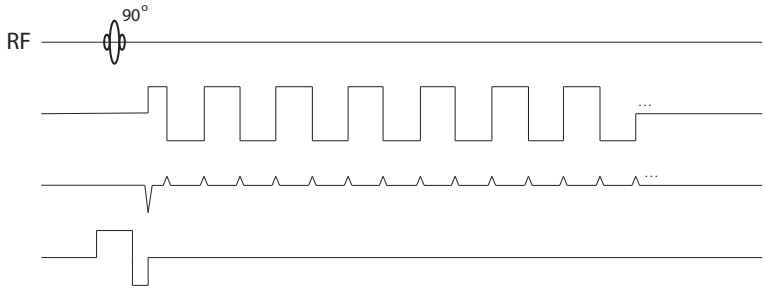


**Figure 7:** *A gradient-echo-planar imaging pulse sequence.*

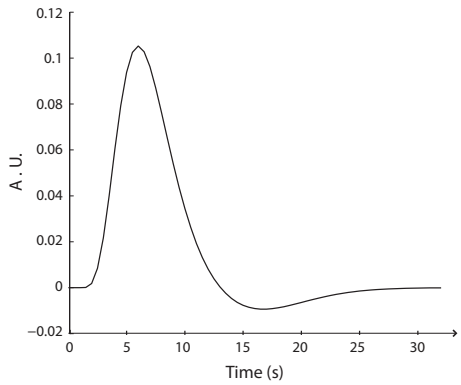


**Figure 8:** *The shape of a typical haemodynamic response to a single short-duration event.*

imaging, the *echo planar imaging* (EPI) sequence, originally developed by Mansfield in 1977 (50). Here, the gradients oscillate so rapidly that all the phase-encoding steps required for an image can be measured after a single excitation. Thus the whole $k$-space is filled after each RF pulse.

Fast scanning enables the detection of functional changes in the brain, but it impairs the spatial resolution. EPI images have low signal-to-noise ratio and the contrast between different tissues is poor. Therefore, high resolution structural MRI images are often acquired so that statistical maps of the functional images can be superimposed on them to better pinpoint the activation sites.

### 5.7.3 The haemodynamic response

The change in the dynamics of the BOLD signal triggered by neuronal activity is called the *haemodynamic response* (HDR). The shape of the HDR can vary in different brain areas and between individuals (51). The first observable HDR changes occur with a 1–2 s lag with respect to the neuronal events that initiate it. The HDR is typically modeled with a canonical *haemodynamic response function* (HRF), shown in Figure 8 to a single short-duration event (occurring at $t = 0$) and modeled as a gamma-variate function.

An initial negative dip may precede the response (52; 53) and it has been attributed to a transient increase in the amount of deoxygenated blood. The initial dip is however often not separately modeled. After a short latency the signal rises, because more oxygen is brought to the area than is extracted by the neurons. The signal reaches its peak at about 5 s. If the stimulus lasts for a longer time, the peak is extended to a plateau. About 6 seconds after the peak, the signal decreases below baseline. The poststimulus undershoot results from faster decrease of blood flow than blood volume after the neuronal activity has returned to baseline. Thus, the relative amount of deoxygenated blood increases and the fMRI signal is reduced below baseline levels. When the blood volume slowly returns to normal level, the signal rises back to baseline.

# 6 Analysis of fMRI data

This section focuses on the analysis of fMRI data. First, the typical image preprocessing necessary prior statistical analysis is explained. Then the most widely used method for determining brain activation in fMRI, the general-linear-model (GLM) based analysis, is introduced. Finally, the data-driven methods used in this work are presented, concentrating mainly on independent component analysis.

## 6.1 Pre-processing of images

The BOLD images are noisy and suffer from several types of artifacts, such as head movements. In addition, the images acquired from different subjects are not directly suitable for group analysis. Thus, careful preprocessing is necessary before the analysis. This section explains the main pre-processing steps implemented in the SPM8 software, which was used in this work.

### 6.1.1 Slice-timing correction

Because the slices in a volume are acquired at slightly different times, the measured signal has a sampling delay in each slice. To correct for this error, the data are often *retimed*. This is usually done by temporal interpolation, which uses information from nearby time points to estimate the amplitude of the signal at the onset of the TR. No retiming was however applied to the data of this work due to a quite modest TR (2.015 s).

### 6.1.2 Realignment

Head motion is probably the most damaging artifact in fMRI. If the head moves during scanning, the signal from a given voxel will be from different parts of the brain in succeeding images. Head-motion-related artifacts are corrected by *realigning* the images. The images are coregistered to a single reference volume using a *rigid body transformation*, which assumes that the shape of the head does not change and corrects for rotations and translations along the $x$-, $y$- and $z$-axes. In spatial registration, the parameters that either maximise or minimize some objective function, such as sum of squared differences, are estimated and then applied to the images.

### 6.1.3 Coregistration

The functional images are coregistered to the structural images from the same subject to facilitate the mapping of low-contrast functional data on high-resolution and high-contrast anatomical images. The coregistration of functional images to structural ones differs from motion correction in two ways. First, the head may not be the same shape in the structural and functional images. Thus, instead of a rigid-body transformation, non-linear transformations are used. Second, the intensity values are different in these two types of images. Therefore, simple cost functions, such as

the sum of squared differences, are not appropriate. For example, *mutual information* can be used as a cost function in functional-structural image coregistration.

### 6.1.4 Spatial normalization

The shape and size of the head varies remarkably across individuals. For group analysis or for averaging effects across subjects, the brains in the images are *normalized* into a standard coordinate system, such as the Talairach space or the Montreal Neurological Institute (MNI) space. In SPM, the procedure has two steps. The first step is a 12-parameter affine transformation to match the size and position of the images. The second step is a non-linear affine transformation, which is modeled by linear combinations of three-dimensional smooth discrete cosine basis functions. The parameters of this non-linear transformation can be found for example within a Bayesian framework, which estimates the most likely regional deformations and then combines them with the global transformations.

### 6.1.5 Spatial smoothing

*Spatial smoothing* reduces the high-frequency spatial components and "blurs" the images. The smoothing is commonly done by spatially low pass filtering the data with a Gaussian filter. Smoothing improves the signal-to-noise ratio and the validity of statistical analysis by making the error distribution more normal. It also decreases the differences across subjects in the sites of brain activations.

## 6.2 The general linear model

To examine real activations in the low-resolution fMRI images, the data are subjected to statistical analysis. The most common way is to use the GLM-based analysis. To find brain areas most affected by the stimulus, a reference time course is constructed by convolving the stimulation time course with a haemodynamic response function. This reference time course is then inserted into the GLM as a *covariate*. The basic idea is that the observed data $x$ can be modeled as a weighted sum of several covariates $g_i$:

$$x = \beta_1 g_1 + \beta_2 g_2 + ... + \beta_n g_n + \epsilon, \tag{18}$$

where $\beta_i$ are the parameter weights, which tell how much each covariate contributes to the overall data, and $\epsilon$ is the error term. For different conditions, a time course can be modeled for each one separately. Known sources of variability, such as head movement or respiration, can also be added as nuisance covariates to improve the validity of the GLM. After the model has been constructed, the weights are approximated by least-squares estimation. The statistical significance of the estimated weights can be tested with $t$-statistics. The analysis can be extended to group level by inserting the individual contrast images into a random-effects analysis to reveal brain areas that are statistically significantly activated in the whole group of subjects.

The use of the GLM requires that the responses can be predicted and a reference time course can be formed. If we want to reveal brain activations during more naturalistic conditions, where the stimulus is multimodal and highly unpredictable, GLM is no longer feasible for the analysis. Purely data-driven approaches, such as inter-subject correlation or independent component analysis, need no a priori models of the stimulus-related activations, and are thus sometimes more suitable for analyzing fMRI data acquired during naturalistic stimulus presentation.

## 6.3 Inter-subject correlation

Inter-subject correlation analysis, proposed by Hasson et al (39), is a data-driven model-free approach for analyzing fMRI data. With ISC it is possible to reveal brain areas whose temporal behaviour is similar across subjects during continuous and complex stimulus presentation, such as watching movies. ISC uses the signal of one subject to model the signal in the corresponding voxels for other subjects by correlating the time series. The signals are correlated voxel by voxel for each subject pair. The correlation maps for all subject pairs are then subjected for group-analysis by testing for significance, for example with a *t*-test. ISC has been shown to segregate *e.g.* the extrinsic, stimulus-driven brain networks from the intrinsic, spontaneous BOLD-signal fluctuations (35; 54).

## 6.4 Seed-based correlation

In seed-based correlation, the measured signal from a pre-defined seed point is correlated with signals from other voxels of the brain to reveal brain areas that are functionally connected with this seed point. The analysis can be extended to group level by subjecting the individual connectivity maps for statistical analysis.

## 6.5 Independent component analysis

This section is mostly based on the tutorial paper on ICA by Hyvärinen *et al.* (55).

### 6.5.1 Motivation

Let's start with a popular simple example to describe what ICA is. Imagine two people speaking in a room and two microphones recording their speech. The signals recorded with the microphones are mixtures of these two speech signals. With ICA, it is possible to estimate the original source signals—the two speech signals—from the mixture signals recorded with the microphones. The mixing of the two speech signals depends on many factors, such as the locations of the microphones and the acoustic properties of the environment. If this mixing would be known, separating the two signals would be easy and could be done by classical methods. However, both the mixing and the original source signals are often unknown and we only have the recorded signals, which makes the problem difficult. One approach for solving the problem is to use some information about the statistical properties of the source

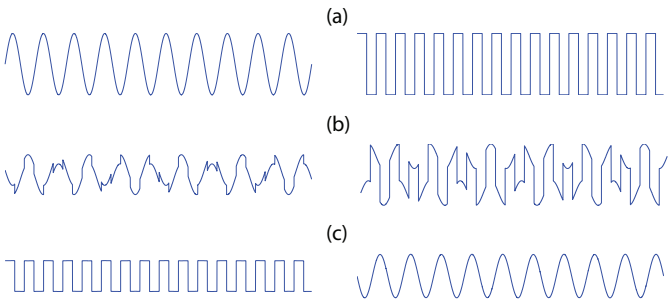


**Figure 9:** *A simple example on how ICA works. (a) The original signals, (b) two mixed observations of the source signals, and (c) the source signals estimated with ICA. These independent components match very well the original signals, with only small differences in scales and signs. FastICA on own simulated data.*

signals to estimate the mixing. ICA is based on the assumption that the source signals are statistically independent. This assumption is often tenable, and actually does not have to hold exactly for ICA to work (55). ICA can be implemented by many algorithms, such as Infomax (28) and FastICA (56). Figure 9 shows a simple example on how ICA separates two source signals from two mixed signals. In fMRI, the mixed signals are the acquired BOLD signals and the source signals are temporally/spatially independent brain networks.

### 6.5.2 Definition of ICA

ICA is an approach for solving the blind source-separation problem, which is the problem of separating the original signals from a set of mixed signals without information (or with very little information) about the source signals or the mixing process. The ICA model is formulated as a generative linear latent-variables model. Latent means that the independent components cannot be directly observed. Generative means that the model describes how well the observed data are generated by a process of mixing the components. When the data are represented by a random vector $\mathbf{x}$ and the independent components by $\mathbf{s}$, the mixing can be expressed in matrix form as

$$\mathbf{x} = \mathbf{A}\mathbf{s}, \tag{19}$$

where $\mathbf{A}$ includes the mixing weights $a_i$ and is therefore called the mixing matrix. The ICA model assumes that the components are statistically independent and have non-gaussian distributions. In practice, the ICs are obtained by estimating the inverse matrix $\mathbf{W} = \mathbf{A}^{-1}$

$$\mathbf{s} = \mathbf{W}\mathbf{x}. \tag{20}$$

### 6.5.3 Measures of non-gaussianity

ICA estimates the independent components by maximizing an objective function, which measures nongaussianity. Measures of nongaussianity are for example kurtosis and negentropy. Kurtosis is estimated by using the fourth-order statistical moment and is defined as

$$kurt(\mathbf{s}) = E\left\{\mathbf{s}^4\right\} - 3E\left\{\mathbf{s}^2\right\}^2, \tag{21}$$

where $E\{\cdot\}$ stands for the expectation value. Kurtosis is simple to compute, but it is very sensitive to outliers (57).

Another measure of nongaussianity is negentropy, which is based on the informationtheoretic quantity of entropy $H$, which in turn is a measure of uncertainty. The entropy of a random variable is larger than that of a structured and predictable one. Since gaussian variables have the largest entropy among all random variables with equal variance (58), minimizing entropy corresponds to maximizing nongaussianity. Negentropy can be considered as negative entropy, and it is defined as

$$J(\mathbf{s}) = H(\mathbf{s}_{gauss}) - H(\mathbf{s}), \tag{22}$$

where $\mathbf{s}_{gauss}$ is a gaussian random variable with the same covariance matrix as $\mathbf{s}$. Negentropy is zero for gaussian variables and always non-negative. Calculating the negentropy according to its definition is computationally difficult and in practice approximations are used.

Another approach for ICA estimation is to minimize mutual information. Mutual information $I$ gives the amount of information shared between random variables and is defined as

$$I(\mathbf{s}_1, \mathbf{s}_2, ...) = \sum_i (H(\mathbf{s}_i) - H(\mathbf{s})). \tag{23}$$

Mutual information is closely related to negentropy. ICA estimation by minimizing mutual information is equivalent to maximizing the sum of nongaussianities of the estimates.

Independent components can be estimated for example with the algorithm called FastICA (56), which was used in this work. It uses negentropy as an objective function and a fixed point optimization scheme based on Newton-iteration.

### 6.5.4 Preprocessing for ICA and order estimation

Before estimating the independent components, some further preprocessing has to be done. The observed data are centered (made zero mean) and whitened (uncorrelated and normalized). Whitening can be done for example with principal component analysis (PCA) (59). PCA transforms the possibly correlated variables into uncorrelated variables called *principal components*. The components are ordered so that the first principal component explains most of the variance of the data. Each succeeding component accounts for as much of the remaining variability as possible.

One way of finding the principal components is to use the eigenvalue decomposition (EVD) of the covariance matrix $E\left\{\widetilde{\mathbf{x}}\widetilde{\mathbf{x}}^T\right\}$ of the data:

$$E\left\{\widetilde{\mathbf{x}}\widetilde{\mathbf{x}}^T\right\} = \mathbf{E}\mathbf{D}\mathbf{E}^T, \tag{24}$$

where $\mathbf{E}$ is the orthogonal matrix of eigenvectors of the covariance matrix and $\mathbf{D}$ is the diagonal matrix of its eigenvalues. The data can now be whitened

$$\widetilde{\mathbf{x}} = \mathbf{E}\mathbf{D}^{-1/2}\mathbf{E}^T\mathbf{x}. \tag{25}$$

Whitening transforms the mixing matrix $\mathbf{A}$ into a new one, $\widetilde{\mathbf{A}}$, and the whitened ICA model can be written as

$$\widetilde{\mathbf{x}} = \mathbf{E}\mathbf{D}^{-1/2}\mathbf{E}^T\mathbf{A}\mathbf{s} = \widetilde{\mathbf{A}}\mathbf{s}. \tag{26}$$

Since $\widetilde{\mathbf{A}}$ is orthogonal, whitening reduces the amount of parameters to be estimated. The dimension of the data can be reduced by leaving out the weakest principal components. This often improves the signal-to-noise ratio and reduces the risk of overfitting, which is sometimes observed in ICA (56). The right number of true components is not known, but several methods exist to estimate it. The minimum description length (MDL) criterion, which was used in this work, is based on the minimum code length (60). The MDL criterion for order selection is

$$E_{MDL}(k) = -L(\mathbf{x}|\Theta_k) + \frac{1}{2}G(\Theta_k)\log N, \tag{27}$$

where $L(\mathbf{x}|\Theta_k)$ is the maximum log-likelihood of the observations, *i.e.* the measured signals $\mathbf{x}$, based on model parameters $\Theta_k$ of the $k$th order and $G(\Theta_k)$ is the penalty term for model complexity given by the total number of free parameters in $\Theta_k$ and $N$ is the number of samples (in case of fMRI images, the samples are the voxels). The maximum log-likelihood is given by (43)

$$L(\mathbf{x}|\Theta_k) = \frac{N}{2}\log\left(\frac{\prod_{i=k+1}^{T}\lambda_i^{1/(T-k)}}{\frac{1}{T-k}\sum_{i=k+1}^{T}\lambda_i}\right)^{T-k}, \tag{28}$$

where $T$ is the original dimension of the multivariate data and $\lambda_i$ is the $i$th eigenvalue of the covariance matrix $E\left\{\widetilde{\mathbf{x}}\widetilde{\mathbf{x}}^T\right\}$ of the measured data. The number of free parameters is given by (43)

$$G(\Theta_k) = 1 + Tk - \frac{1}{2}k(k-1). \tag{29}$$

Estimating too few components leads to loss of information. On the other hand, overestimation could result in splitting of the informative components and in spurious components due to unconstrained estimation and factorization that will overfit the data (10).

### 6.5.5 Ambiguities of ICA

ICA has two main ambiguities. First, the signs and scales of the sources cannot be identified. Second, the ICs do not appear in any specific order. What is more, all ICA algorithms converge to slightly different results in separate runs.

### 6.5.6 ICASSO

ICASSO (61) is an algorithm for investigating the reliability of the components. ICASSO runs ICA several times with different initial values and/or with differently bootstrapped data sets. The estimated components are clustered according to a similarity measure, such as absolute correlation. The stability index of the ICA-estimate clusters is computed as the difference between intra-cluster similarities and average extra-cluster similarities, and it provides a quantative estimate of the compactness of the clusters. If the stability index is close to unity, ICA estimation is stable and consistent, meaning that similar components are estimated at every run of the algorithm. The tighter the cluster a component belongs to is, the more reliable the IC is. The most unreliable components do not belong to any cluster. The cluster centers represent the ideal components. ICASSO was used in this work, since it is inbuilt in the group-ICA toolbox (62) that was used for ICA analysis. However, also other methods for estimating the consistency of ICs exist (63; 64).

### 6.5.7 Application of ICA to fMRI data

ICA is well suited for analyzing fMRI data, since both activity-related signals and noise match the assumptions and limitations of ICA (29). One advantage of using ICA in fMRI data analysis is that it separates some of the noise sources as independent components (29; 65).

Spatial ICA is typically used in the analysis of fMRI data. Spatial ICA finds systematically non-overlapping brain networks without constraining the temporal domain. In the spatial model, the rows of the data matrix contain the images and the columns are the voxels. The rows of $\mathbf{S}$ are the spatially independent components. The columns of the mixing matrix $\mathbf{A}$ contain the weights, *i.e.* the time courses of the spatial ICs.

### 6.5.8 Group ICA

ICA analysis can be extended to group level. Calhoun *et al.* (62) proposed a method for performing group ICA, which was also used in this work. The first step is data reduction, which can be done in either two or three stages. First the dimension of each subject's functional data is reduced. Then, the data from all subjects are concatenated together and the dimension of this aggregate data set is reduced. The reduced aggregate data matrix $\mathbf{X}$ is then (62)

$$\mathbf{X} = \mathbf{G}^{-1} \begin{bmatrix} \mathbf{F_1^{-1}X_1} \\ \cdot \\ \cdot \\ \mathbf{F_M^{-1}X_M} \end{bmatrix} \tag{30}$$

where M is the number of subjects and $\mathbf{G}^{-1}$ and $\mathbf{F}_i^{-1}$ are the reducing matrices from PCA for the concatenated data set and for subject $i$, respectively. $\mathbf{X_i}$ represents the original data matrix from subject $i$, in which one row contains one volume of fMRI data. Alternatively, the subjects can be divided into groups of which the dimension is decreased before the final data reduction. The next step is to apply ICA to the reduced data set. The mixing matrix can further be partitioned according to individuals and the ICA model can then be written as

$$\begin{bmatrix} \mathbf{G_1} \\ \cdot \\ \cdot \\ \mathbf{G_M} \end{bmatrix} \hat{\mathbf{A}}\hat{\mathbf{S}} = \begin{bmatrix} \mathbf{F_1^{-1}X_1} \\ \cdot \\ \cdot \\ \mathbf{F_M^{-1}X_M} \end{bmatrix}, \tag{31}$$

where $\hat{\mathbf{A}}$ is the mixing matrix for the group data and $\hat{\mathbf{S}}$ is the component map. The individual subject components $\hat{\mathbf{S}}_i$ can be also reconstructed utilizing the matrices $\mathbf{G}$ and $\mathbf{F}$:

$$\hat{\mathbf{S}}_\mathbf{i} = (\mathbf{G_i}\hat{\mathbf{A}})^{-1}\mathbf{F_i^{-1}X_i}. \tag{32}$$

The ICs of individual subjects can be used for calculating the mean components and for $t$-statistics. Both the group components and the individual subject components can be scaled for visualization using percent signal change or $z$-scores.

# 7 Materials and methods

## 7.1 Subjects

Twenty two healthy volunteers (9 females, 6 males, mean age 24 years, range 19–49 years) participated in the study after written informed consent. The study had prior approval by the Ethics Committee of Helsinki and Uusimaa Hospital District. Altogether, the data from 7 subjects were rejected because of technical problems, drowsiness of the subject or excessive head movements; thus, the following analyses are based on data of 15 subjects.

## 7.2 Stimuli

During fMRI scanning, the subjects viewed a 15-min silent film (At Land by Maya Deren, 1944). The film was followed by a 44-s long compressed version of the film. This summarization consisted of 22 2-s episodes from the film selected by means of an automatic video summarization algorithm (66). The algorithm analyzed low level features and the selection was additionally weighted by face and movement detection. The summarization was preceded and followed by 20-s resting periods, during which the subjects were asked to fixate on a cross. Otherwise, the subjects' task was simply to watch the movie and the summarization. Figure 10 illustrates the order and durations of the stimuli. The stimuli were delivered using the Presentation software (version 0.81, `http://www.neurobehavioralsystems.com`). Videos were projected (projector Vista X3 REV Q, Christie Digital Systems, Canada, Inc.) to a transparent screen placed behind the subjects, which the subjects viewed via a mirror.

## 7.3 Data acquisition

The fMRI images were acquired with a Sigma VH/I 3.0 T MRI scanner (General Electric, Milwaukee, WI, USA). Functional images were obtained using gradient echo-planar-imaging sequence with following parameters: TR 2.015 s, TE 32 ms,

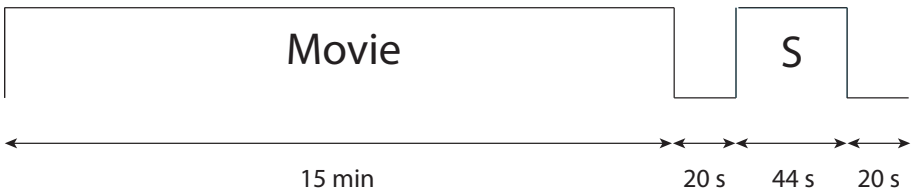


**Figure 10:** *The order of stimuli. The 15 min long movie was followed by a 44-s summarization (S) of the movie.*

FA 75°, 34 oblique axial slices, slice thickness 4 mm, matrix $64 \times 64$, voxel size $3 \times 3 \times 3$ mm, field of view (FOV) 22 cm. Altogether 485 volumes were collected. These volumes included 4 dummy scans (the first scans that were acquired to ensure that a spin system was in a steady state before data collection), which were removed from further analysis. Structural images were scanned with 3-D T1 spoiled gradient imaging, matrix 256 x 256, TR 10 ms, TE 3 s, flip angle 15°, preparation time 300 ms, FOV 25.6 cm, slice thickness 1 mm, number of excitations 1. Movements of the subject's right eye were followed with SMI MEye Track long-range eye tracking system (Sensomotoric Instruments GmbH, Germany), based on video-oculography and the dark pupil-corneal reflection method. The eye-tracking data were not utilized in this thesis.

## 7.4 Pre-processing

The fMRI data were preprocessed using SPM8 software (`http://www.fil.ion.ucl.ac.uk/spm/software/spm8/`), including realignment, co-registration, normalization into MNI space and smoothing with a 6-mm (full-width half maximum) Gaussian filter. Before normalization, the images were skull-stripped using the FreeSurfer software (`http://surfer.nmr.mgh.harvard.edu/`).

## 7.5 ICA

The IC analysis was performed with the GIFT software (version v2.0d, `http://icatb.sourceforge.net/groupica.htm`) for group-ICA. The number of sources was estimated to be 70 using the minimum description length algorithm inbuilt in GIFT. Twenty five, 40 and 70 ICs were calculated with the Fast ICA algorithm. ICASSO analysis was done to confirm the reliability of the components. Three ICs, representing the sensorimotor, dorsal attention and default-mode networks, were selected by visual inspection from the 25-component decomposition. From the decompositions of 40 and 70 components, respectively, ICs were selected by visual inspection so that they together resembled the spatial maps of the selected ICs from the 25 component decomposition. The selection was facilitated by spatially correlating the unthresholded spatial maps with the three 25-component maps. Most of the selected subcomponents belonged to the eight ICs with highest correlation coefficients. The correlations between the time courses of the selected components were computed.

## 7.6 Sorting of components using inter-subject correlation

The ISC map, revealing the brain areas that are activated temporally similarly across subjects, has been shown to include extrinsic, stimulus-driven brain networks (35; 54). Malinen and Hari (67) introduced an approach for spatial sorting of ICs on the basis of ISC maps to find the most stimulus-driven ICs. This approach was utilized also in this work. First, the ISC map identified the brain regions that were most related to the external stimuli. The ICs in each decomposition were

sorted according to the spatial overlap with the thresholded ISC map (threshold at $p = 10^{-7}$; corrected for family wise error, FWE; minimum cluster size 150 voxels). The sorting parameter was defined as the equally weighted sum of the Pearson's correlation coefficients between the thresholded ISC map and the mean ICs and the amount of overlapping voxels relative to the total amount of voxels. The amount of overlapping voxels was determined from binary images, where the value of voxels exceeding a certain threshold was set to 1 and for the others to 0. Also, the time series of the components that were most related to the stimulus were compared with events in the movie.

## 7.7 Seed-based correlation

The seed-based correlation was done utilizing the SPM8 software. The aim was to see whether the areas of the independent components ${}^{\mathrm{sm}}_{25}$IC10, ${}^{\mathrm{att}}_{25}$IC11 and ${}^{\mathrm{def}}_{25}$IC17, representing the sensorimotor, dorsal attention and default mode networks, really were functionally connected. In the notation used, the superscript refers to the network (att = attention, def = default, sm = sensorimotor) and the subscript to the decomposition to which the component belongs (25, 40 or 70 components). Three seed points were determined on the basis of the ICA results by subjecting the individual ICs to group analysis (one sample $t$-test, $p < 0.001$ uncorrected) and selecting a voxel with high statistical significance ($p < 10^{-4}$ uncorrected) as the center for the seed-point (a sphere with 6-mm radius). For ${}^{\mathrm{att}}_{25}$IC11 the seed point was near the IPS (MNI coordinates –24 –76 37) and for ${}^{\mathrm{def}}_{25}$IC17 on the PCC (0 –55 22). With this criteria, the seed point for ${}^{\mathrm{sm}}_{25}$IC10 lied on the right supratemporal auditory cortex (54 –10 7). Because this area was not located on the sensorimotor cortex, another seed point was selected from the right hand area in the left hemisphere, in the "precentral knob" (68) (–37 –24 61, calculated as an average from coordinates reported in earlier studies (69–72)). The mean pre-processed signals from these areas were extracted for each individual with the MarsBaR software (`http://marsbar.sourceforge.net/`). Each extracted time course was used as a regressor in a GLM analysis to reveal the individual connectivity maps. These maps were then subjected to a one sample $t$-test.

# 8 Results

## 8.1 Brain areas comprising the sensorimotor network

Figure 11a shows the spatial maps and Figure 11b the time courses of the selected ICs for the sensorimotor network in each decomposition.

${}^{\text{sm}}_{25}$IC10 corresponds to the sensorimotor network: it covers bilaterally the primary motor cortex (MI), the supplementary motor area (SMA) and the primary somatosensory (SI) cortices bilaterally. It also covers the Sylvian fissure overlapping with the secondary somatosensory (SII) and auditory cortices in both hemispheres.

In the 40-component decomposition, three subcomponents—${}^{\text{sm}}_{40}$IC5, ${}^{\text{sm}}_{40}$IC7 and ${}^{\text{sm}}_{40}$IC32, shown in Figure 11a—cover the spatial map of ${}^{\text{sm}}_{25}$IC10. Of these, ${}^{\text{sm}}_{40}$IC32 was flipped, and therefore its spatial map and the corresponding time course were multiplied by –1 for visualization. This IC includes bilaterally the superior MI and SI and the SMA in the medial surface of the brain. ${}^{\text{sm}}_{40}$IC5 covers the inferior part of the primary sensorimotor cortex bilaterally. ${}^{\text{sm}}_{40}$IC7 includes parts of the secondary somatosensory cortex as well as parts of the auditory cortex in both hemispheres.

In the 70-component decomposition, ${}^{\text{sm}}_{25}$IC10 is split into four subcomponents: ${}^{\text{sm}}_{70}$IC35, ${}^{\text{sm}}_{70}$IC41, ${}^{\text{sm}}_{70}$IC1, and ${}^{\text{sm}}_{70}$IC15. ${}^{\text{sm}}_{70}$IC35 comprises the supplementary motor area and bilaterally the most superior parts of the primary sensorimotor cortex. ${}^{\text{sm}}_{70}$IC41 covers bilaterally the superior part of the primary sensorimotor cortex. Together these two components roughly correspond to ${}^{\text{sm}}_{40}$IC32. ${}^{\text{sm}}_{70}$IC1 encompasses the inferior part of the primary sensorimotor cortex and corresponds to ${}^{\text{sm}}_{40}$IC5. ${}^{\text{sm}}_{70}$IC15 covers the SII and the supratemporal auditory cortex and is about the same as ${}^{\text{sm}}_{40}$IC7.

Figure 11c shows the splitting of the components in the sensorimotor network and lists the related brain areas in detail.

## 8.2 Brain areas comprising the attention network

Figure 12a illustrates the spatial maps and Figure 12b the time courses of the selected ICs for the attention network.

${}^{\text{att}}_{25}$IC11 corresponds to the attention network: it covers bilaterally the intraparietal sulcus (IPS), the junctions of the precentral and superior frontal gyri (the FEFs) as well as inferior temporal areas. In addition, occipital visual areas, the fusiform gyri, as well as the superior parts of the cerebellum are within this IC.

Two ICs in the 40-component decomposition—${}^{\text{att}}_{40}$IC38 and ${}^{\text{att}}_{40}$IC15—cover attention-related brain areas. ${}^{\text{att}}_{40}$IC38 covers bilaterally the IPS, the FEFs, the middle temporal areas, and some additional areas. In general, ${}^{\text{att}}_{40}$IC38 covers more superior areas than ${}^{\text{att}}_{25}$IC11. However, the superior areas became visible also in the spatial map of ${}^{\text{att}}_{25}$IC11 when the threshold was decreased to $z = 0.5$. ${}^{\text{att}}_{40}$IC15 closely resembles the spatial map of ${}^{\text{att}}_{25}$IC11.

In the 70-component decomposition the attention network is mostly related to the five subcomponents shown in Figure 12a. ${}^{\text{att}}_{70}$IC43 shows bilaterally the IPS and the FEFs. It resembles ${}^{\text{att}}_{40}$IC38. ${}^{\text{att}}_{70}$IC67 is more lateralized to the right hemisphere, and it extends bilaterally over the inferior IPS and parietal areas. ${}^{\text{att}}_{70}$IC50 is similar

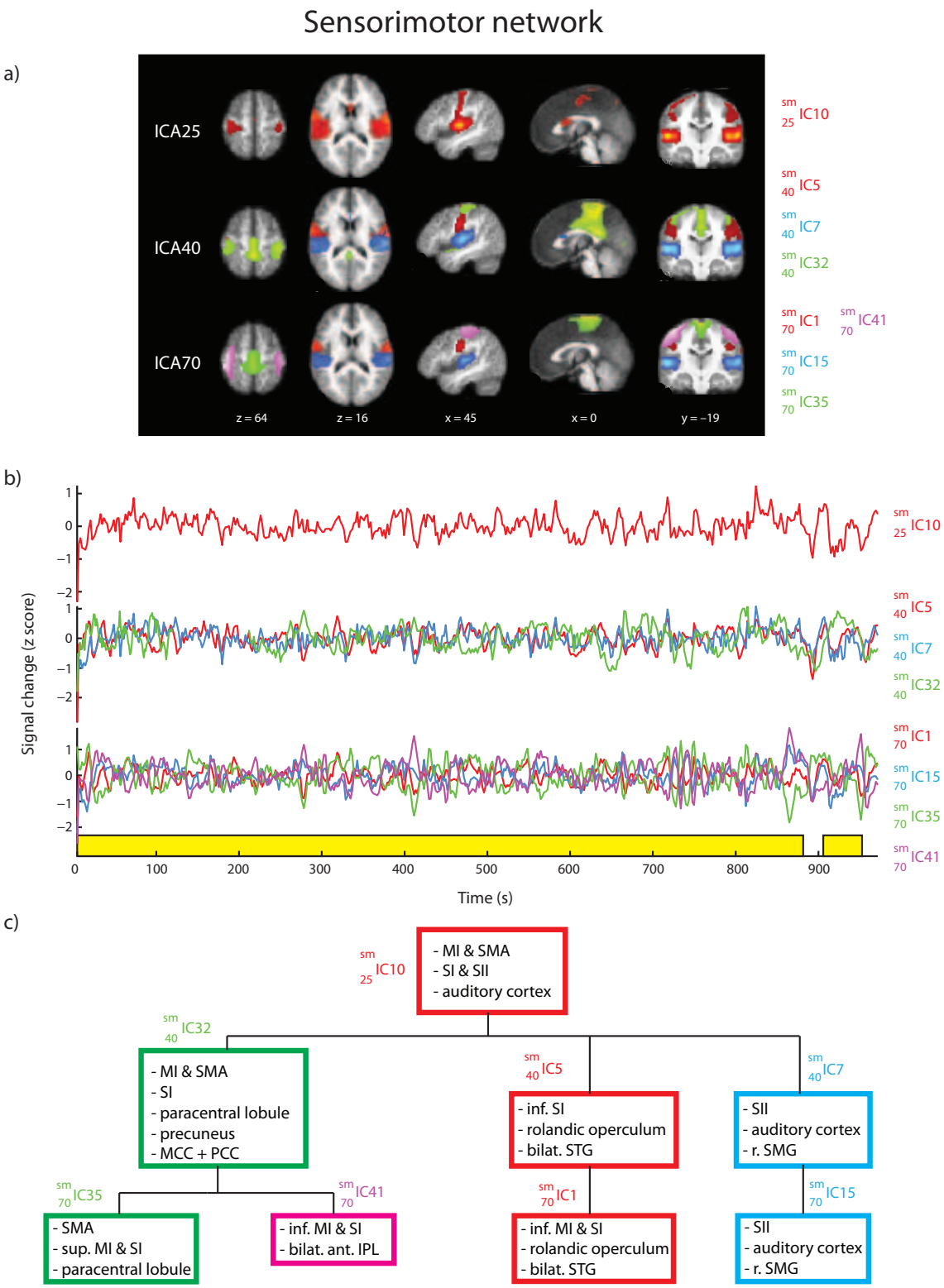


**Figure 11:** *a) The spatial maps and b) the time courses of the ICs selected to represent the sensorimotor network in each decomposition. The spatial maps are thresholded at z = 1.5 for the 25-IC decomposition, at z = 2.0 for the 40-IC decomposition and at z = 2.5 for the 70-IC decomposition. c) The splitting of the components. MI = primary motor area, SMA = supplementary motor area, SI = primary somatosensory area, SII = secondary somatosensory area, MCC = middle cingulate cortex, PCC = posterior cingulate cortex, STG = superior temporal gyrus (part of the auditory cortex), SMG = supramarginal gyrus, IPL = inferior parietal lobe. The parts of the auditory cortex covered by* ${}^{\text{sm}}_{25}$IC10, ${}^{\text{sm}}_{40}$IC7 *and* ${}^{\text{sm}}_{70}$IC15 *include bilaterally the supratemporal auditory cortex.*

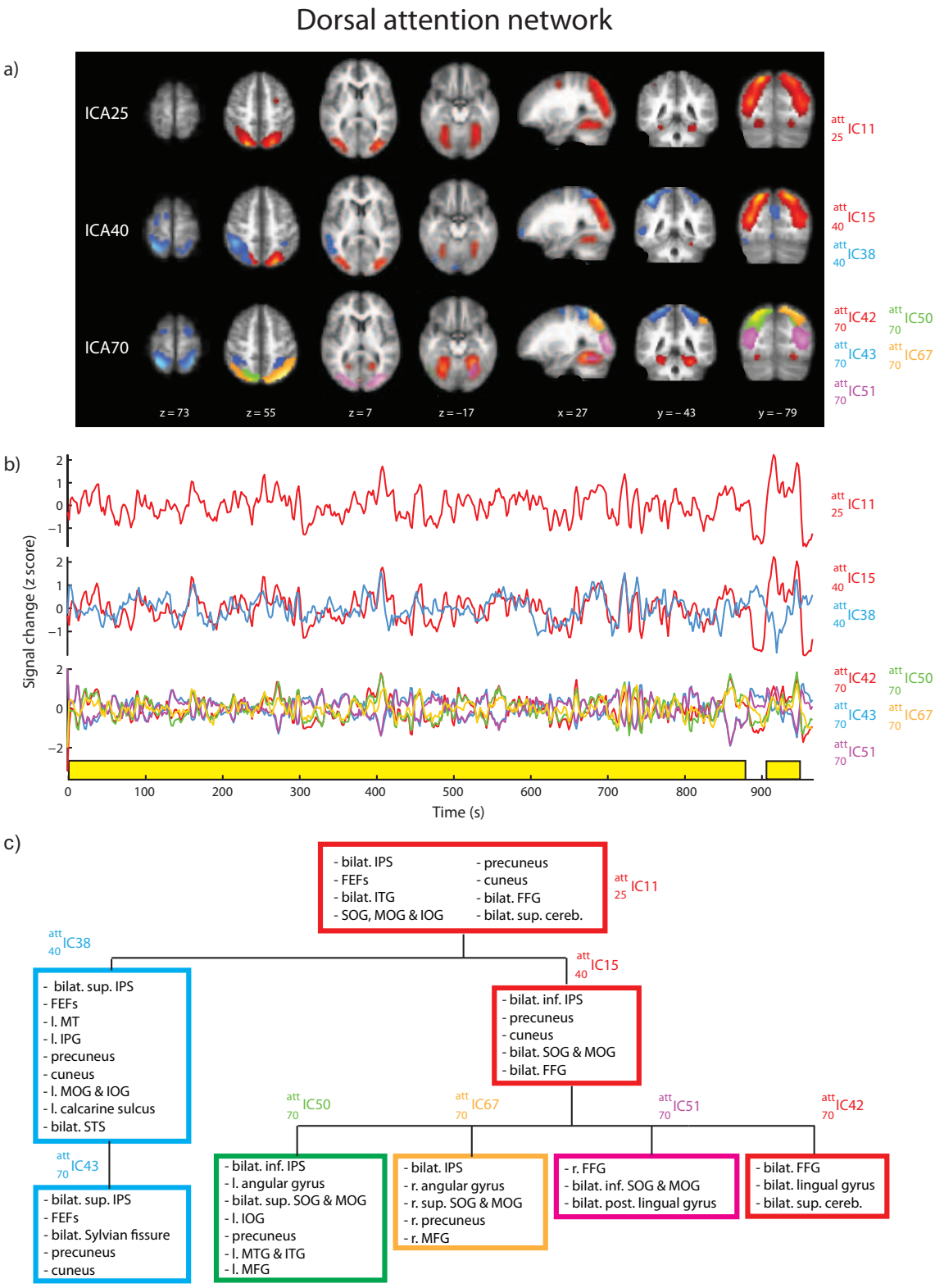


**Figure 12:** *a) The spatial maps and b) the time courses of the ICs selected to represent the dorsal attention network in each decomposition. The spatial maps are thresholded at z = 1.5 for the 25-IC decomposition, at z = 2.0 for the 40-IC decomposition and at z = 2.5. for the 70-IC decomposition. c) The splitting of the components. IPS = intraparietal sulcus, FEF = frontal eye field (the junction of the precentral and superior frontal gyrus), ITG = inferior temporal gyrus, FFG = fusiform gyrus, MT = middle temporal area, IPG = inferior parietal gyrus, SOG = superior occipital gyrus, MOG = middle occipital gyrus, IOG = inferior occipital gyrus, STS = superior temporal sulcus, MTG = middle temporal gyrus, ITG = inferior temporal gyrus, MFG = middle frontal gyrus.*

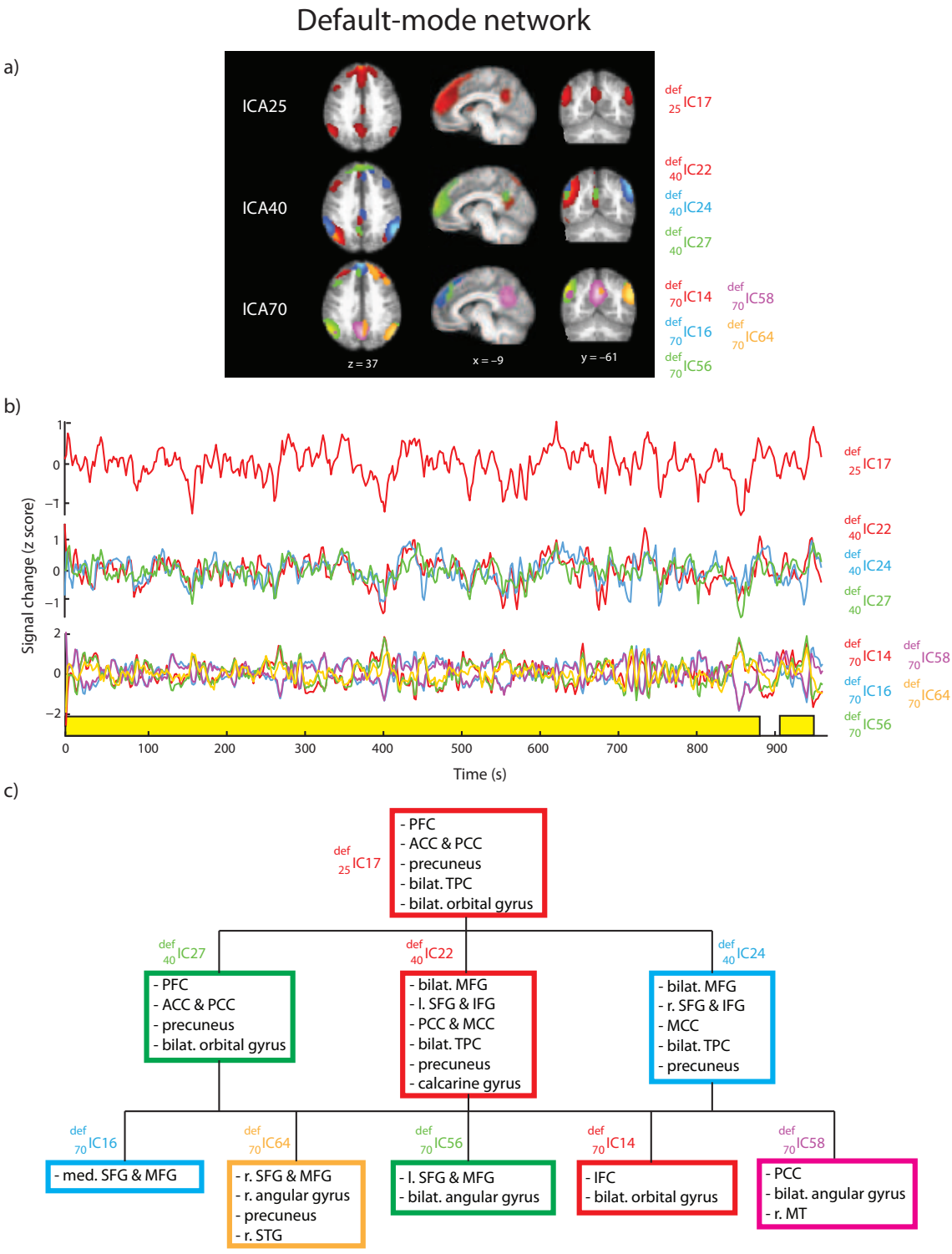


**Figure 13:** *a) The spatial maps and b) the time courses of the ICs selected to represent the default-mode network in each decomposition. The spatial maps are thresholded at z = 1.5 for the 25-IC decomposition, at z = 2.0 for the 40-IC decomposition and at z = 2.5. for the 70-IC decomposition. c) The splitting of the components. PFC = prefrontal cortex, ACC = anterior cingulate cortex, TPC = temporoparietal cortex (including MTG and STG, the superior and inferior parietal gyrus, the angular gyrus and the SMG), SFG = superior frontal gyrus, IFG = inferior frontal gyrus, IFC = inferior frontal cortex, MT = middle temporal area.*

to ${}^{\text{att}}_{70}$IC67, but is lateralized to the left hemisphere. ${}^{\text{att}}_{70}$IC51 covers mainly occipital visual areas. ${}^{\text{att}}_{70}$IC42 coincides bilaterally with the fusiform and lingual gyri as well as superior parts of the cerebellum. Together ${}^{\text{att}}_{70}$IC67, ${}^{\text{att}}_{70}$IC50, ${}^{\text{att}}_{70}$IC51 and ${}^{\text{att}}_{70}$IC42 cover the spatial map of ${}^{\text{att}}_{40}$IC15.

Figure 12c lists the splitting and related brain areas in detail.

## 8.3 Brain areas comprising the default-mode network

Figure 13a shows the spatial maps and Figure 13b the time courses of the selected ICs for the default-mode network in each decomposition.

${}^{\text{def}}_{25}$IC17 represents the default mode network, covering parts of the posterior and anterior cingulate cortices (PCC and ACC), the precuneus, medial prefrontal cortex, and bilaterally parts on the temporoparietal cortex. It also extends bilaterally over the lateral orbital gyrus.

The default mode component ${}^{\text{def}}_{25}$IC17 is split into 3 partly overlapping subcomponents in the 40-component decomposition (Figure 13a). ${}^{\text{def}}_{40}$IC27 is concentrated on the medial prefrontal cortex. ${}^{\text{def}}_{40}$IC22 and ${}^{\text{def}}_{40}$IC24 look quite similar, ${}^{\text{def}}_{40}$IC22 is just more lateralized to the left and ${}^{\text{def}}_{40}$IC24 to the right. Together these components cover parts of the frontal cortex, the PCC, bilaterally parts of the temporoparietal cortex, the precuneus and the calcarine gyrus.

In the 70-component decomposition, ${}^{\text{def}}_{25}$IC17 is split into five subcomponents shown in Figure 13a. ${}^{\text{def}}_{70}$IC16 comprises the medial parts of the prefrontal cortex. ${}^{\text{def}}_{70}$IC64 is lateralized on the right hemisphere and covers parts of the right prefrontal cortex, the right side of the precuneus and areas on the right temporoparietal cortex. ${}^{\text{def}}_{70}$IC56 is similar to ${}^{\text{def}}_{70}$IC64, but lateralized to the left hemisphere. ${}^{\text{def}}_{70}$IC14 includes the inferior parts of the frontal cortex. ${}^{\text{def}}_{70}$IC58 is concentrated on the PCC.

Figure 13c illustrates the splitting and related brain areas in detail.

## 8.4 ICASSO results

Figure 14 illustrates the 2D curvilinear component analysis projections of the clustered ICASSO-based ICA estimates. Small and tight clusters correspond to similar component estimates at every run. The background color of a cluster indicates the average intra-cluster similarity. At the dimensionality of 25, the clusters are tight and well separated and all clusters have an intra-cluster similarity greater than 0.8. When the dimensionality is increased to 40, some of the clusters start to overlap and four clusters have an intra-cluster similarity less than 0.8. At the dimensionality of 70, a large portion of the clusters distributed in the center of the graph overlap considerably and several clusters have an intra-cluster similarity lower than 0.8. Thus the ICA estimation starts to become less stable at high dimensionalities.

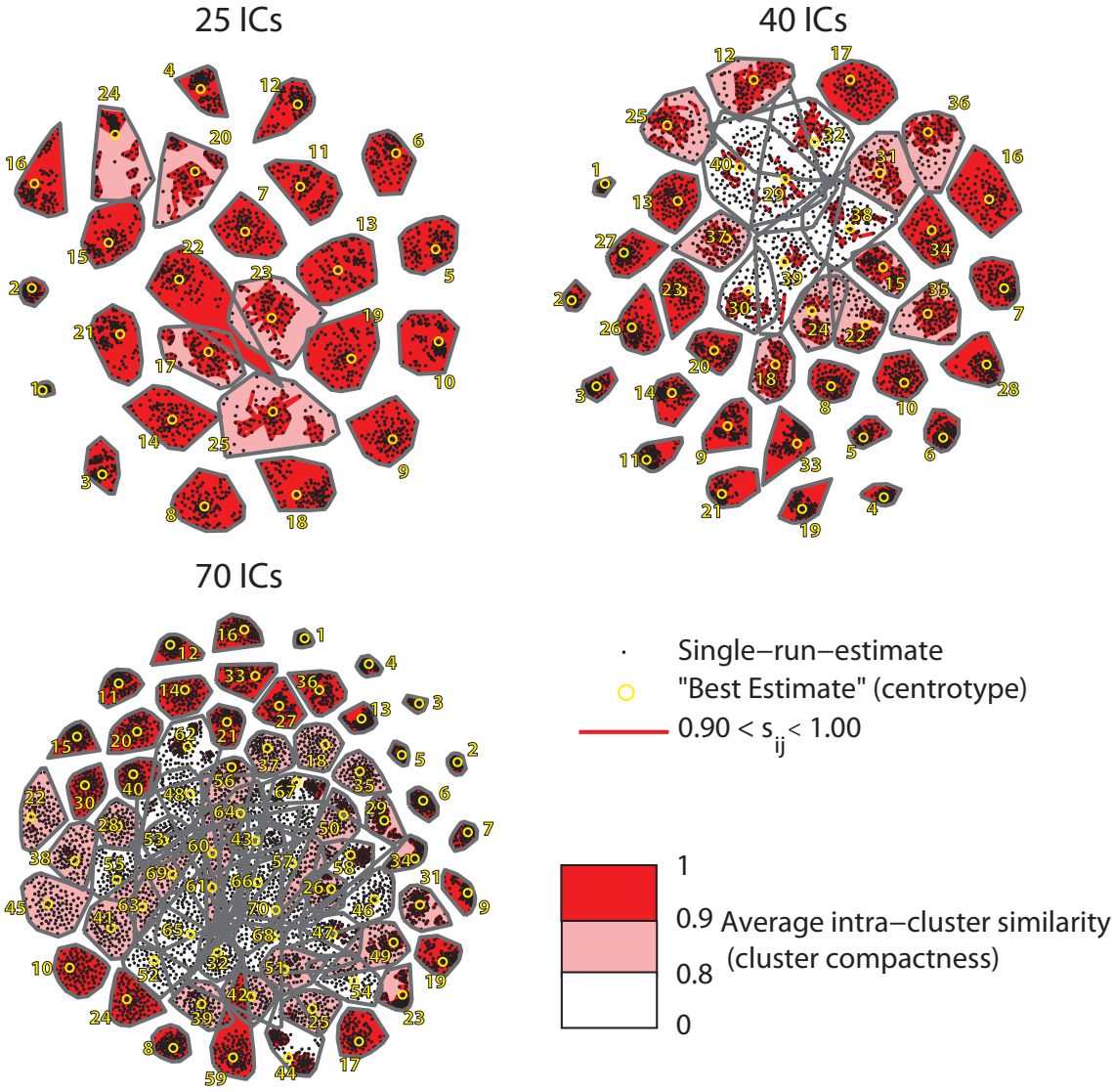


**Figure 14:** *The 2D curvilinear component analysis projections of the clustered IC estimates in each decomposition. The number of a cluster refers to the IC number. Note that the pairwise similarities* $s_{ij}$ *are not plotted if the average intra-cluster similarity is over 0.9.*

## 8.5 IC time courses

### 8.5.1 Correlations between the IC time courses

Figure 15 illustrates the correlation matrix for the selected components. The solid lines segregate the decompositions of 25, 40 and 70 components from each other. The dashed lines separate the components belonging to the sensorimotor, dorsal attention and default-mode networks, respectively. The correlations explained in more detail below are highlighted with white circles/ellipses and indicated with capital letters (A–R). Also the spatial maps of the ICs of the 70-component decomposition are illustrated. All correlations mentioned hereafter are statistically significant ($p <$

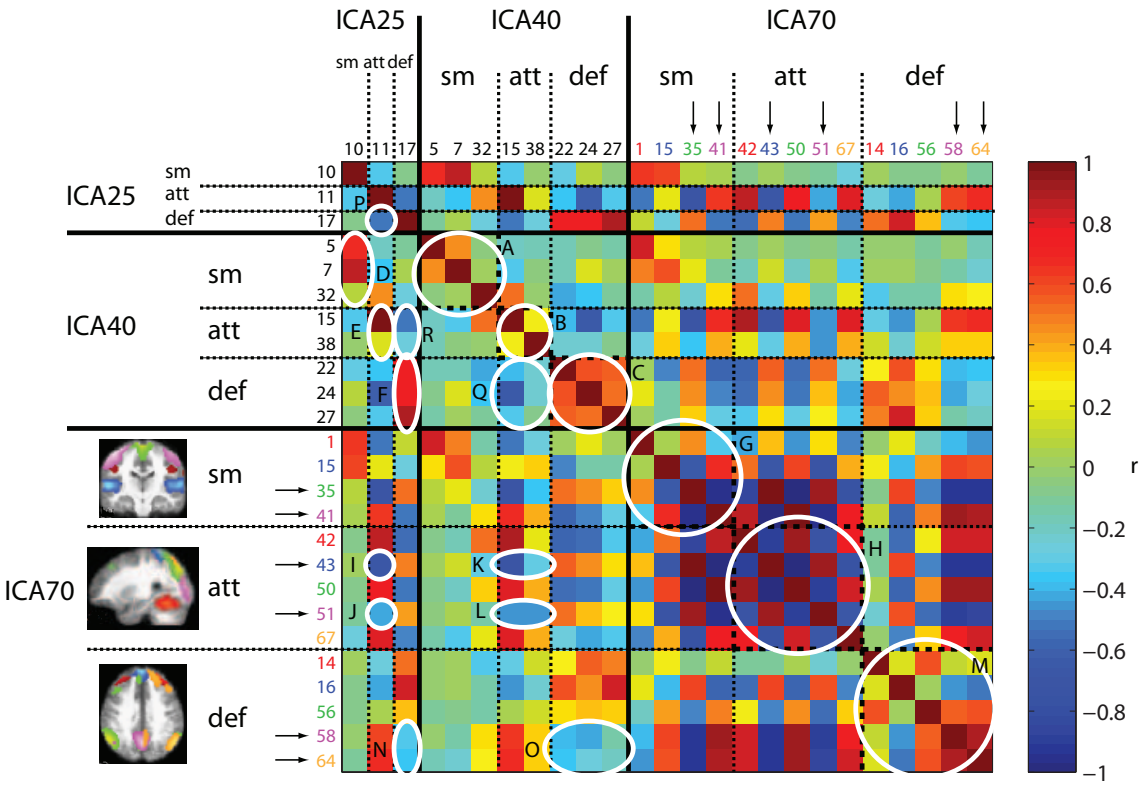


**Figure 15:** *The correlation matrix of all the selected components. The solid lines segregate the decompositions of 25, 40 and 70 components from each other. The dashed lines separate the components belonging to the sensorimotor, dorsal attention and default mode network, respectively. The areas encircled with white and labeled with capital letters are explained in more detail in the text. The components, whose time courses match the mean extracted fMRI signal badly (from top to bottom* ${}^{\mathrm{sm}}_{70}$IC35,${}^{\mathrm{sm}}_{70}$ IC41,${}^{\mathrm{att}}_{70}$ IC43,${}^{\mathrm{att}}_{70}$ IC51,${}^{\mathrm{def}}_{70}$ IC58 *and* ${}^{\mathrm{def}}_{70}$IC64*) are indicated with arrows.*

$10^{-3}$).

In the 40-component decomposition, the subcomponents belonging to the same network correlate positively with each other (A–C), except for ${}^{\mathrm{sm}}_{40}$IC32, whose time course correlates very weakly with the other 40-IC sensorimotor components (A) and it does not correlate statistically significantly with the time course of ${}^{\mathrm{sm}}_{25}$IC10 (D). The time courses of ${}^{\mathrm{att}}_{40}$IC15 and ${}^{\mathrm{att}}_{25}$IC11 are strongly positively correlated ($r = 0.99$) (E). ${}^{\mathrm{att}}_{40}$IC38 correlates modestly with ${}^{\mathrm{att}}_{25}$IC11 ($r = 0.18$) (E). The ICs of the default-mode network in the 40-component decomposition correlate positively with ${}^{\mathrm{def}}_{25}$IC17 (F).

In the sensorimotor network, the time course of ${}^{\mathrm{sm}}_{70}$IC41 correlates negatively with its neighbouring components ${}^{\mathrm{sm}}_{70}$IC35 ($r = -0.96$) and ${}^{\mathrm{sm}}_{70}$IC1 ($r = -0.33$) and positively with the time course of ${}^{\mathrm{sm}}_{70}$IC15 ($r = 0.68$). ${}^{\mathrm{sm}}_{70}$IC35 correlates negatively with ${}^{\mathrm{sm}}_{70}$IC15 ($r = -0.63$) and positively with ${}^{\mathrm{sm}}_{70}$IC1 ($r = 0.44$). (G)

Within the attention network, ${}^{\mathrm{att}}_{70}$IC43 and ${}^{\mathrm{att}}_{70}$IC51 correlate positively with each other ($r = 0.94$) and negatively with the other components neighbouring them (H).

The time courses of ${}^{\text{att}}_{70}$IC43 and ${}^{\text{att}}_{70}$IC51 also correlate negatively with the time courses of the components belonging to the attention network in the lower dimensionalities (I–L).

Within the default-mode network, ${}^{\text{def}}_{70}$IC16 has a negative correlation with ${}^{\text{def}}_{70}$IC58 ($r = -0.45$) and ${}^{\text{def}}_{70}$IC64 ($r = -0.50$) (M). ${}^{\text{def}}_{70}$IC58 and ${}^{\text{def}}_{70}$IC64 correlate negatively with the selected default mode components in the 25- and 40-component decompositions (N,O).

In general, components of the attention network correlate negatively with the ICs of the default mode network within and across the decompositions, except for the ICs in the 70-component set (P–R).

### 8.5.2 IC time courses and the extracted fMRI signal

As noted above and seen in Figure 15, the time courses of some neighbouring ICs in the 70-IC decomposition correlate negatively with each other. Because strong negative temporal correlation between neighbouring brain areas is physiologically unlikely, the original preprocessed fMRI data were extracted from the areas of the ICs from each subject to see how well the IC time courses match with the actual signal. The regions of interest (ROIs) were spheres of 6-mm radius with the center at the highest peak of the $t$-maps of each component. The correlations between the ROI-signals and the time courses of corresponding individual IC time courses were computed. Figure 16 shows the mean ($\pm$ standard deviation) correlation for each

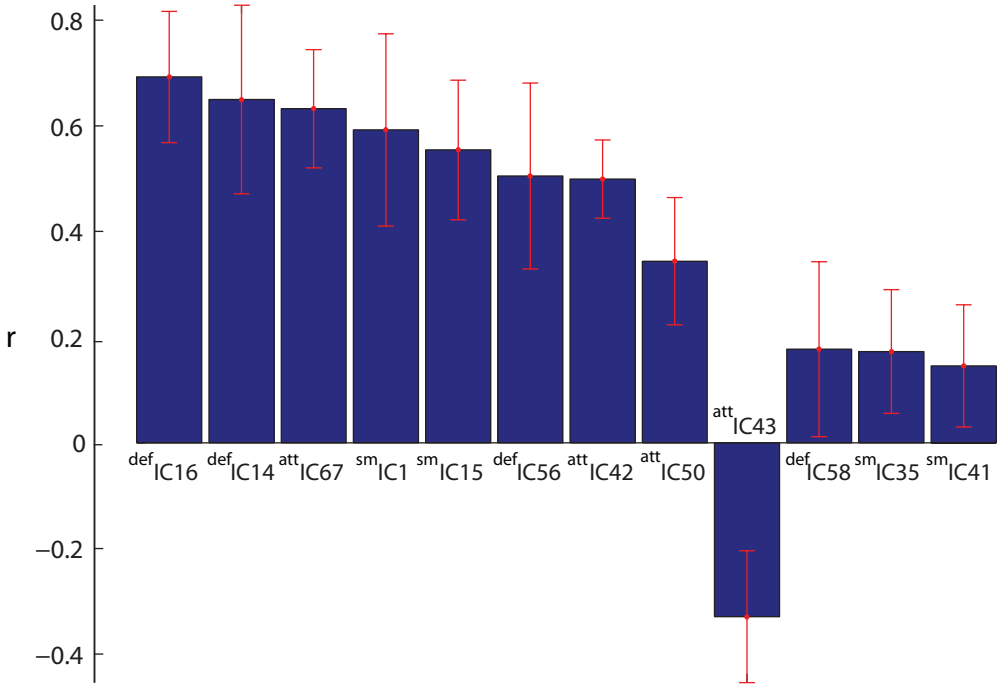


**Figure 16:** *The mean correlations and standard deviations between the time courses of the selected components in the 70-IC decomposition and the extracted BOLD signals. Only statistically significant correlations are shown ($p < 0.05$).*

component.

Two components did not have statistically significant correlation with the ROI-signal ($^{\text{att}}_{70}$IC51 and $^{\text{def}}_{70}$IC64; not shown in the Figure 16) and three ICs ($^{\text{sm}}_{70}$IC41, $^{\text{sm}}_{70}$IC35 and $^{\text{def}}_{70}$IC58) have only a weak correlation with the extracted signal. One component of the attention network ($^{\text{att}}_{70}$IC43) correlates negatively with the extracted signal ($r = -0.33 \pm 0.12$), indicating that the time course of this IC was flipped. These six ICs with spurious time courses are indicated with arrows in Figure 15.

## 8.6 Single-subject ICA

Since the time course of $^{\text{att}}_{70}$IC43 was most probably flipped, this IC was further examined. ICA was performed for each subject individually to see whether the IC time courses get distorted only in group ICA or in ICA in general. Seventy components were estimated for each subject and an IC corresponding to $^{\text{att}}_{70}$IC43 was selected according to best spatial correlation. The correlations between the time courses of these selected components and the mean time course of $^{\text{att}}_{70}$IC43 were then computed. For two subjects, no significant correlation was found and for the rest of the subjects, the correlation was negative (mean $r = -0.31 \pm 0.17$), meaning that the flipping occurred only in group ICA.

## 8.7 ICASSO analysis with subjects in different concatenation order

It has recently been shown that the subject concatenation order can affect the output of GIFT (73). Therefore, the group ICA analysis with ICASSO was repeated by giving the subjects' data in a different order into GIFT. Spatial correlation was used to match the ICs between the first and second ICASSO analysis. The correlations between the time courses of these ICs were then computed similarly as was done for the first data order.

Figure 17 shows the correlation matrices of the time courses in the 70-IC decompositions. Clearly, the matrices for the first and second ICASSO analysis differ. Notably, with the second data order, neighbouring components do not correlate negatively with each other, as was the case for the first data order. Still, the time course of the component corresponding to $^{\text{att}}_{70}$IC43 correlates negatively with the other attention-related components. Also the time course of the IC corresponding to $^{\text{sm}}_{70}$IC41 has only weak correlation with the other sensorimotor components. The IC corresponding to $^{\text{def}}_{70}$IC58 is the only default component that does not correlate negatively with the ICs of the attention network. It still correlates positively with the other default components.

## 8.8 IC ordering using the ISC map

Figure 18a shows the ISC map used to sort the ICs (thresholded at $p = 10^{-7}$ FWE-corrected, minimum cluster size 150 voxels). The map covers bilaterally the

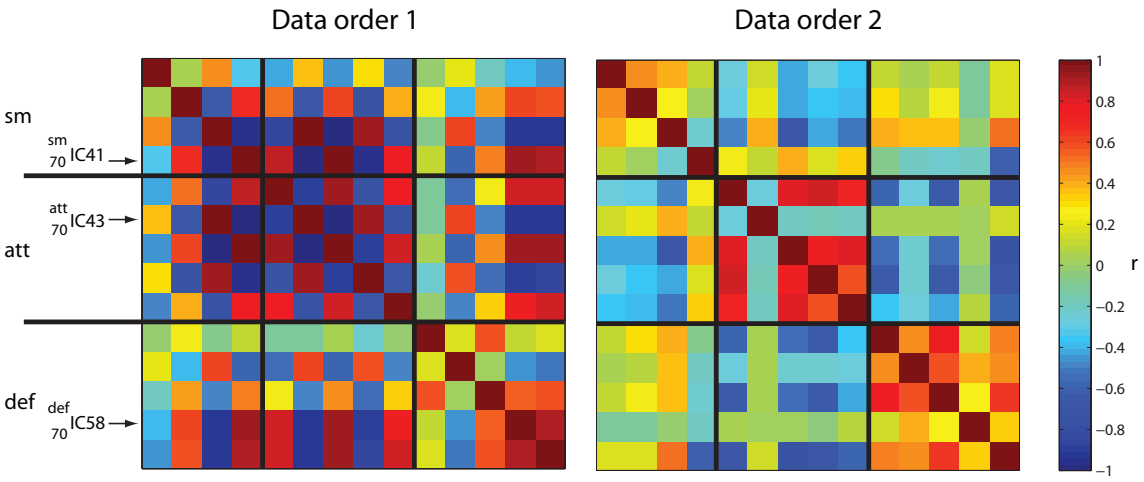


**Figure 17:** *The correlation matrices of the time courses of the ICs of the 70 component decompositions for the ICASSO analysis with subjects' data in two different concatenation orders (data order 1, data order 2).*

visual areas in the occipital lobe, the middle and inferior frontal areas bilaterally, the temporal lobes, precentral gyri, bilaterally the IPS and the FEFs, parts of the supplementary motor area and cingulate cortex, the precuneus, cuneus, the hippocampi and parahippocampal gyri, fusiform and lingual gyri, basal ganglia and superior parts of the cerebellum.

The spatial maps of the components in each decomposition were ordered according to the spatial overlap with the ISC map to find out which of the ICs were most related to the stimuli. Figure 18b shows the sorting parameters for the ICs in each decomposition. Components covering the visual cortex had high sorting parameter values as expected for the silent video stimulus. Also the components belonging to the attention network spatially overlapped the ISC map. Instead, the sensorimotor and default-mode ICs had only a minor spatial overlap with the ISC map.

## 8.9 Relation to events in the movie

Since the ISC map suggested that only the visual and attention components were closely related to the stimuli, the time courses of these components, only, were compared with events in the movie by taking into account the typical haemodynamic lag of 6 seconds. Because the reliability of the time courses of the components in the 70-IC set was uncertain, components in the 40-IC set were evaluated. ${}^{\text{att}}_{40}$IC38 covered bilaterally the IPS and the FEFs. Because ${}^{\text{att}}_{40}$IC15 included higher order visual areas, also one component comprising the primary visual area (${}^{\text{vis}}_{40}$IC21) but not belonging to the attention network was included in the analysis.

Figure 19 illustrates the time courses of these three components with scenes associated with maxima and minima of the time courses. The time courses of ${}^{\text{att}}_{40}$IC38 and ${}^{\text{att}}_{40}$IC15 are very similar. Interestingly, most of the peaks coincide with hand action or hand movement. The visual component ${}^{\text{vis}}_{40}$IC21 does not peak at all of these time instants. The movie and the summarization are illustrated in Figure

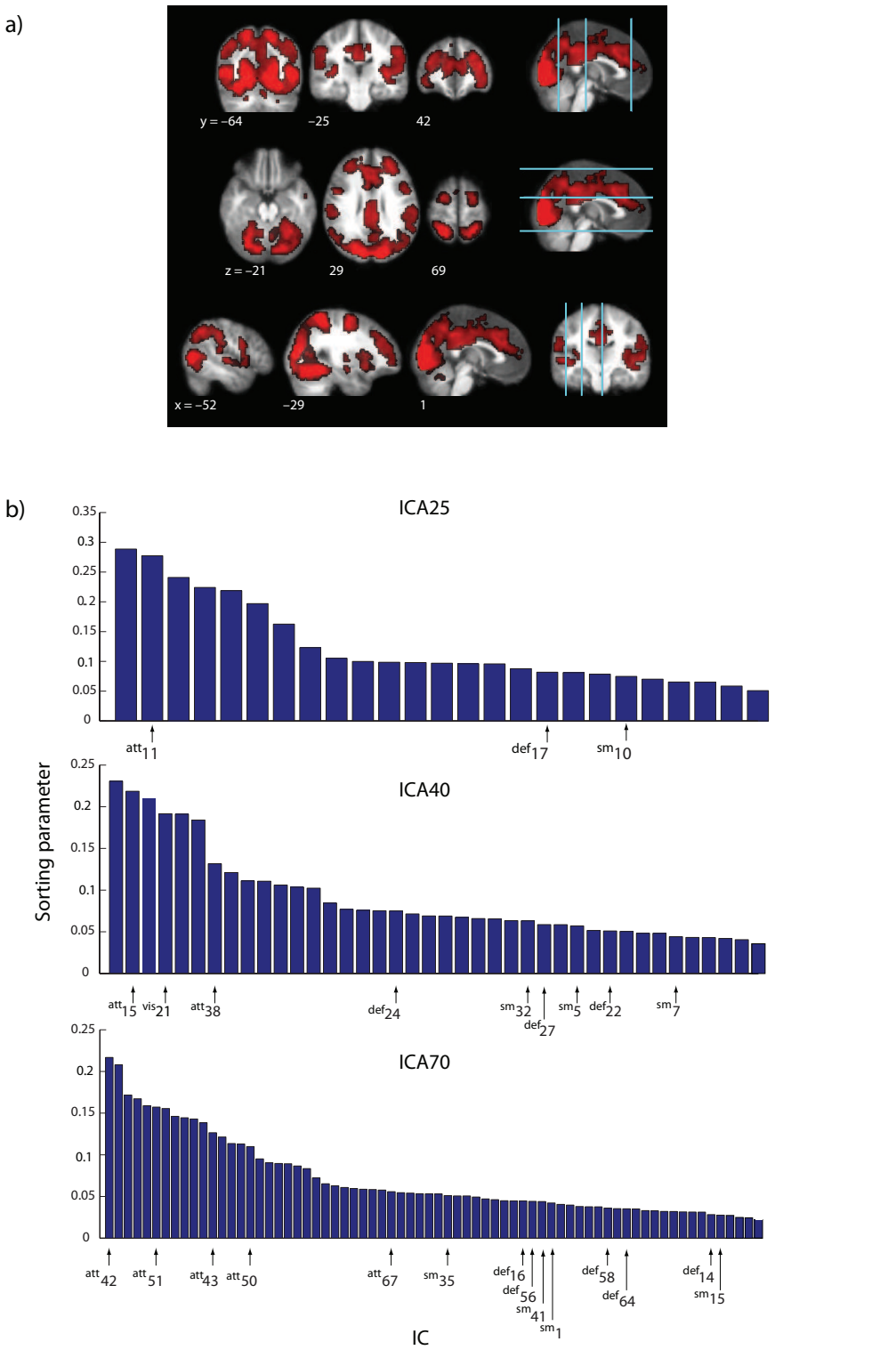


**Figure 18:** *a) The ISC map used for sorting the ICs. b) The sorting parameters of the ICs ordered from the most to the least overlap with the ISC map in each decomposition.*

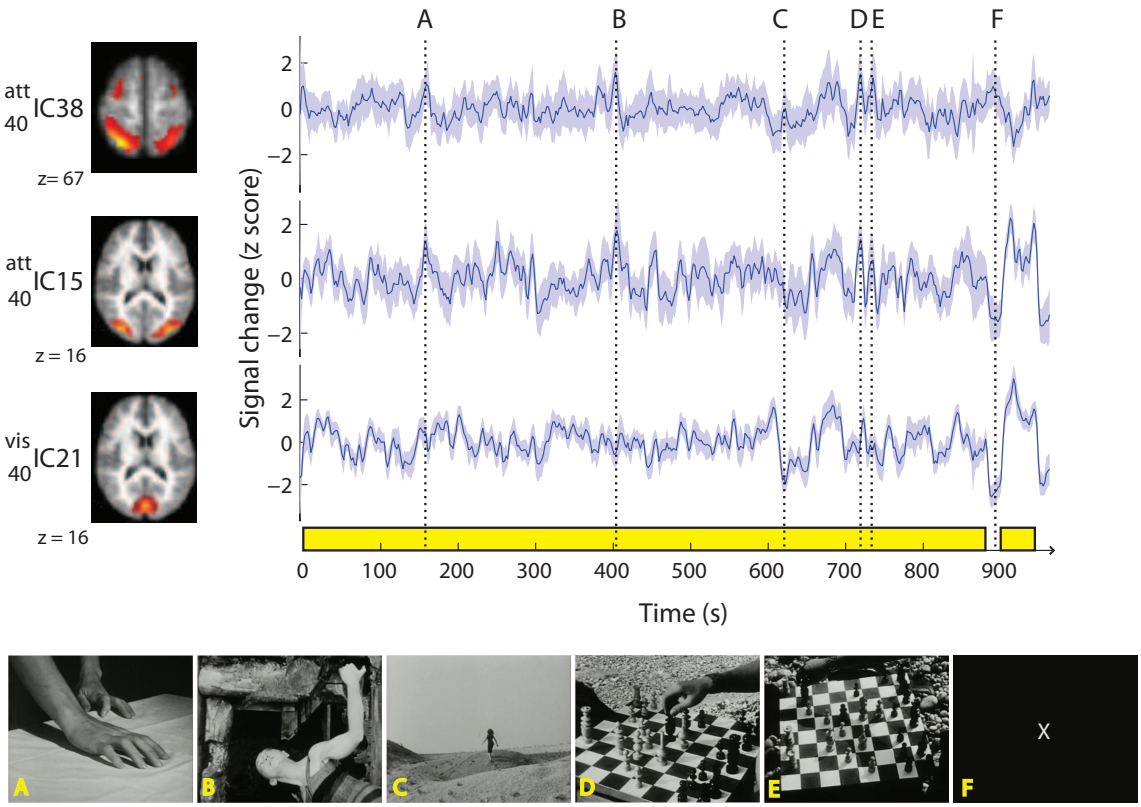


**Figure 19:** *The two uppermost traces show the mean±STD time courses of the two ICs of the 40-IC decomposition belonging to the attention network. The lowest trace shows the time course of a component comprising the early visual cortex but not belonging to the attention network. The yellow bars indicate the timing and duration of the movie followed by the summarization. Below the time courses are examples of movie scenes associated with peak activity indicated by vertical lines in the time courses.*

19 with yellow bars on the time axis. The end of the movie (at $t = 884$ s), the period with no visual stimulation ($t = 884$–$904$ s) and the beginning ($t = 904$ s) and end ($t = 948$ s) of the summarization can clearly be distinguished in the time courses of ${}^{\text{att}}_{40}$IC15 and ${}^{\text{vis}}_{40}$IC21, but not so obviously in ${}^{\text{att}}_{40}$IC38. ${}^{\text{att}}_{40}$IC15 includes also visual areas but ${}^{\text{att}}_{40}$IC38 does not, so the existence of visual stimulation affects more the time course of ${}^{\text{att}}_{40}$IC15. The activity of the visual component ${}^{\text{vis}}_{40}$IC21 decreases during scenes with little details, for example during a scene of a desert.

## 8.10 Seed-based correlation

Figure 20 illustrates the correlation maps produced using four seed points. All maps are thresholded at $p = 0.01$ (FWE-corrected).

The correlation map for the seed region located in the IPS (cluster threshold 100 voxels) shows bilaterally the IPS, parts of the parietal cortex, the right FEF and the middle temporal areas, all known to belong to the dorsal attention network

and also covered by ${}^{\text{att}}_{25}$IC11. The correlation map matches well with the spatial map of ${}^{\text{att}}_{25}$IC11 also in other brain areas, such as the visual cortex. In addition, the correlation map covers in both hemispheres the precentral gyrus, the central sulcus, the SMG, the calcarine gyrus, putamen, pallidum, hippocampus and parts of the cerebellum. It also extends to precuneus, cuneus and middle cingulum.

For the seed in the PCC, the correlation map (cluster threshold 50 voxels) covers the same areas as ${}^{\text{def}}_{25}$IC17 and extends also bilaterally to the lingual gyrus and the calcarine gyrus, as well as the left thalamus and caudate.

For the seed in the right hand knob the correlation map (cluster threshold 150 voxels) reveals connectivity between MI, SI, SMA and SII, precuneus, middle cingulum, IPG, parts of the frontal cortex and the rolandic operculum. The map agrees well with the spatial map of ${}^{\text{sm}}_{25}$IC10, except that ${}^{\text{sm}}_{25}$IC10 did not include frontal areas and the correlation map does not reach the auditory cortex. However, the correlation map produced with the seed located on the maximum of the *t*-map of ${}^{\text{sm}}_{25}$IC10 on the right supratemporal auditory cortex (cluster threshold 150 voxels) covers the part of ${}^{\text{sm}}_{25}$IC10 located in the auditory cortex and SII, but does not include any primary motor or somatosensory areas. The map extends to ACC, MCC, thalamus and basal ganglia; the latter areas include relay regions of the motor and sensory circuits.

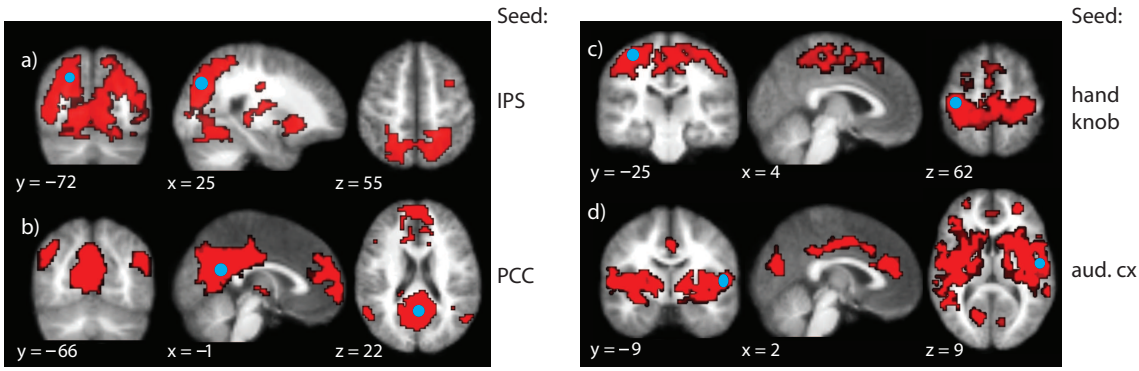


**Figure 20:** *Correlation maps produced using four different seed points: a) local maximum of* ${}^{\text{att}}_{25}$IC11 *in the IPS b) local maximum of* ${}^{\text{def}}_{25}$IC17 *in the PCC c) the motor cortex hand knob in the left hemisphere, and d) global maximum of* ${}^{\text{sm}}_{25}$IC10 *in the right supratemporal auditory cortex. The seed points are shown as blue circles.*

# 9 Discussion and conclusions

In this thesis, three cortical networks, *i.e.* the sensorimotor, dorsal attention and default-mode networks, were examined with ICA, seed-based correlation and ISC applied to fMRI data acquired with a 3-T magnet. The results of ICA and seed-based correlation were compared and the stimulus-related components were identified by examining their spatial overlap with the ISC map. The effect of increasing the number of estimated independent components on the results of group ICA was examined. In addition, the interest was to find out how the activations in the networks were modulated by the movie stimulus.

The three networks were identified with ICA and seed-based correlation from fMRI data collected when subjects were watching a 15-min film ("At Land" by Maya Deren). The results of these two methods resembled each other. The results of ICA differed at the three different dimensionalities. When the dimensionality of ICA was 25, the ICs of the sensorimotor and dorsal attention networks included brain areas that do not belong to the networks as described in the literature. In the 40-IC decomposition, the ICs resembled the previously described sensorimotor and dorsal attention networks (31; 32) without any additional areas, and therefore this dimensionality seemed to be close to the correct one. At dimensionality of 70, the networks split further into smaller subnetworks and peculiarities in the IC time courses appeared. The problem of distorted time courses seemed to be specific to group ICA.

According to the spatial overlap with the ISC map, the visual and attentional ICs were most closely related to the stimulus. The activity of these ICs followed distinct features in the movie. The sensorimotor ICs were not stimulus-related, which was surprising since the movie included a lot of movement and touch, and was expected to activate the sensorimotor cortex.

## 9.1 Effect of the number of ICs on group ICA results

With 25 components the networks were wide-ranging, but still functionally feasible. At this low dimensionality of ICA, additional areas merged to the sensorimotor and attention ICs. The attention-related IC included visual areas, indicating that the activity in these areas was rather similar. Coinciding activation of the attention network and visual areas is reasonable during watching to and concentrating on a silent film. The correlation map produced with the seed in the IPS supported the assumption of functional connectivity, since it matched well with the attention IC that also included visual areas. The ISC map also included areas of the attention network as well as visual areas.

In the 25-IC decomposition, the sensorimotor IC included auditory areas. The SII and parts of the auditory cortex occurred in same IC also when the dimensionality of ICA was increased. That result could be due to the proximity of the SII and the auditory cortex, albeit, audiotactile interactions are known to exist (74–77). In a similar way, the seed-based analysis showed functional connectivity between these areas. In contrast, the seed-point analysis with a seed in the hand motor cortex did

not show any connection between the sensorimotor network and auditory cortex. On the other hand, with the seed in the auditory cortex, the auditory cortex and SII but no primary sensorimotor areas were covered by the correlation map.

When the number of components was increased, the networks split into functionally reasonable subnetworks. Additional areas in the attention and sensorimotor networks were separated from the networks when the dimensionality was increased from 25 to 40. With 70 components, the networks split further into smaller subnetworks. The splitting either resulted in lateralized subnetworks or the networks were separated in the superior-inferior direction. Some functionally meaningful subareas of the networks formed own ICs, such as the PCC in the default-mode network and the SMA in the sensorimotor network.

One IC of the attention network emerged only when the dimensionality was increased to 40. Also in the study of Abou-Elseoud *et al.* (9), where the characteristics of RSN-related ICs at different model orders were studied, new subcomponents emerged at higher model orders. Similarly as here, at low dimensionalities the individual signal sources merged into singular components involving functionally separate units. The authors suggested that a high model-order forces ICA to search for more local non-Gaussianity maxima and therefore the algorithm succeeds better in separating and finding functionally relevant components.

Some of the components did not split any further when the dimensionality was increased from 40 to 70. Also this result agrees with the findings of Abou-Elseoud *et al.* (9), who suggested that the stable components might represent less connected nodes, while the branching ones are kind of connector hubs with lots of connections to other nodes. The stable components, with less connections, are functionally more independent.

When the number of ICs was high (70), some peculiarities occurred in the IC time courses so that a few neighboring components had negative correlations with each other. Such a behaviour is physiologically unlikely and thus most probably was an artifact of the ICA analysis. The distortion was confirmed by the observation that the time courses of all ICs did not match with the raw fMRI signal extracted from the IC maxima. Especially one IC correlated negatively with the extracted signal, indicating that the time course, but not the spatial map of this IC was flipped. Nevertheless, the spatial splitting was still functionally meaningful as it is physiologically feasible that brain networks consist of smaller subnetworks of slightly different function. However, splitting can result from a too high dimensionality of ICA so that the algorithm "forces" areas actually belonging to the same component apart, and thus the time courses of these components get distorted. This result agrees with earlier work of Beckmann and Smith (10), who concluded that estimating too many components causes overfitting and leads to arbitrary splitting of the ICs due to unconstrained estimation.

When the dimensionality of ICA was 40, the additional areas and the networks were separated as distinct ICs. No negative correlations existed between the time courses of ICs covering neighbouring brain areas and no IC time courses got flipped. Thus, 40 likely was closest to the correct dimensionality.

The problem of spurious or flipped time courses at a too high dimensionality was

specific to group ICA, since no peculiarities occurred when ICA was performed at individual level.

Similarly to earlier findings (73), the subject concatenation order affected the outputs of GIFT. Despite slightly different results, the modified subject order still led to spurious or flipped time courses.

The data reduction steps included in the group-ICA estimation might have contributed to the peculiarities of the IC time courses. In this work, data reduction was performed in two stages. First, the data of each subject were compressed with PCA. Then the compressed data from all subjects were concatenated to a big data matrix and the dimensionality of this aggregate data set was reduced. In the first step, the data from each subject were reduced to the same dimensionality (70). Also, the number of retained components was the same in the subject-level and group-level PCA. Erhardt *et al.* (78) compared different group-ICA methods for fMRI data analysis including data reduction, ICA estimation and back reconstruction. Concerning data reduction, they concluded that on one hand, estimating the same number of components in the subject- and group-level retained the greatest information. On the other hand, the estimation quality of the subject-specific IC time courses and spatial maps was better when more components were retained in the subject-level reduction than in the group-level reduction.

The results of this work suggest that the MDL algorithm inbuilt in GIFT overestimated the number of components, since the number of components estimated by MDL (70) resulted in peculiarities in the IC time courses. The MDL criterion is based on the assumption of independent and identically distributed (*i.i.d.*) samples. Li *et al.* (43) suggested that smoothing, a common pre-processing step of fMRI images, weakens the *i.i.d.* assumption. When dependent samples are taken as *i.i.d.*, the MDL criterion tends to overestimate the number of sources. Li and coworkers proposed a subsampling scheme to improve the performance of different information-theoretic criteria, such as MDL. Another factor that might cause the MDL criterion to overestimate the number of sources is the presence of noise in the fMRI signal. Cordes *et al.* (79) introduced another approach for order selection in fMRI data based on an autoregressive noise model. Unlike information-theoretic criteria like MDL, this method takes into account the autocorrelations of noise.

According to the ICASSO results, the repeatability of the ICs decreased when the number of component estimates was increased. With 70 ICs, a large portion of the clusters of the single-run-estimates overlapped considerably. Thus the ICA estimation started to get less stable at a high dimensionality. Significant reduction in ICA repeatability with increasing model order has been reported earlier (9; 43).

## 9.2 Temporal activation patterns of the ICs

According to the ISC map, the visual and attention-related ICs were most stimulus-related of all components. Instead, the components of the default and sensorimotor networks overlapped poorly with the ISC map, indicating that watching the movie did not affect these networks similarly across subjects. On the other hand, most of the sensorimotor components were very stable in the ICASSO analysis. Thus, the

sensorimotor network seemed to have been consistently active, but not significantly affected by the movie, at least not in a similar manner across subjects.

The activation patterns of the visual and attention ICs followed specific features in the movie. The attention-related components were activated especially during hand actions. These components covered the IPS, which has been shown to be activated during watching manual activity (80; 81). It might also be that the activation was driven by attentional processing, when the subjects were consciously following the movements of the hands. The visual component did not peak at these time instants, indicating that the attentional components, although containing some visual areas, were not entirely driven by the visual features.

In general, the time courses of the ICs belonging to the attention network correlated negatively with the time courses of the ICs of the default-mode network. Thus, the activity of the default network decreased during attention-involving processing. This result agrees with earlier studies that have shown deactivation in the brain regions of the default mode network during visual attention (35; 82).

## 9.3 Conclusions

This thesis had two main objectives. The main focus was on examining the effect of increasing the number of components to be estimated on the results of group ICA. Stimulus-related components were identified utilizing the spatial overlap with the ISC map and their activation time courses were compared to events in the movie.

According to the ISC map, the visual ICs and ICs of the dorsal attention network were most stimulus-related and their activation patterns followed distinct features in the movie.

The results of group ICA were different at the three dimensionalities tested. At low dimensionality (25), ICs merged together, but in a meaningful way, possibly providing a general picture of large-scale neuronal networks. The dimensionality of 40 ICs seemed to be closest to the correct one, since at this dimensionality the additional areas were separated from the networks and the IC time courses appeared reliable. At high dimensionality (70), the ICs split into functionally meaningful subcomponents, but peculiarities occurred in the IC time courses, indicating that the number of ICs was too high. This problem did not occur when ICA was performed at individual level, suggesting that the error might be generated either in the PCA or back reconstruction steps involved in group ICA analysis. Erhardt *et al.* (78) compared different group-ICA methods including data reduction, ICA estimation and back reconstruction. The conclusion was that using subject-specific PCA with noise-free ICA with certain back reconstruction method provides the most robust and accurate IC spatial maps and time courses. However, whether the problem of peculiar IC time courses applies only to one or all of the possible combinations of the different PCA and back reconstruction methods and in which step the error occurs are issues that need further examination.

The results of this work contribute to current understanding of how the number of IC estimates affects the outcome of group ICA. The findings could be applied to empirical probing of the correct number of independent sources in group-fMRI data.

# References


[1] Fox, M. D. and Raichle, M. E. (2007) Spontaneous fluctuations in brain activity observed with functional magnetic resonance imaging. *Nat Rev Neurosci*, **8**, 700–11.

[2] Bartels, A. and Zeki, S. (2004) The chronoarchitecture of the human brain–natural viewing conditions reveal a time-based anatomy of the brain. *Neuroimage*, **22**, 419–33.

[3] Bartels, A. and Zeki, S. (2005) Brain dynamics during natural viewing conditions–a new guide for mapping connectivity in vivo. *Neuroimage*, **24**, 339–49.

[4] Hasson, U., Yang, E., Vallines, I., Heeger, D. J., and Rubin, N. (2008) A hierarchy of temporal receptive windows in human cortex. *J Neurosci*, **28**, 2539–50.

[5] Wilson, S. M., Molnar-Szakacs, I., and Iacoboni, M. (2008) Beyond superior temporal cortex: intersubject correlations in narrative speech comprehension. *Cereb Cortex*, **18**, 230–42.

[6] Jääskeläinen, I. P., Koskentalo, K., Balk, M. H., Autti, T., Kauramäki, J., Pomren, C., and Sams, M. (2008) Inter-subject synchronization of prefrontal cortex hemodynamic activity during natural viewing. *Open Neuroimag J*, **2**, 14–9.

[7] Malinen, S., Hlushchuk, Y., and Hari, R. (2007) Towards natural stimulation in fMRI–issues of data analysis. *Neuroimage*, **35**, 131–9.

[8] Smith, S. M., et al. (2009) Correspondence of the brain's functional architecture during activation and rest. *Proc Natl Acad Sci U S A*, **106**, 13040–5.

[9] Abou-Elseoud, A., Starck, T., Remes, J., Nikkinen, J., Tervonen, O., and Kiviniemi, V. (2010) The effect of model order selection in group PICA. *Hum Brain Mapp*, **31**, 1207–1216.

[10] Beckmann, C. F. and Smith, S. M. (2004) Probabilistic independent component analysis for functional magnetic resonance imaging. *IEEE Trans Med Imaging*, **23**, 137–52.

[11] van de Ven, V. G., Formisano, E., Prvulovic, D., Roeder, C. H., and Linden, D. E. (2004) Functional connectivity as revealed by spatial independent component analysis of fMRI measurements during rest. *Hum Brain Mapp*, **22**, 165–78.

[12] Raichle, M. E., MacLeod, A. M., Snyder, A. Z., Powers, W. J., Gusnard, D. A., and Shulman, G. L. (2001) A default mode of brain function. *Proc Natl Acad Sci U S A*, **98**, 676–82.

[13] Shulman, G., Fiez, J., Corbetta, M., Buckner, R., Miezin, F., Raichle, M., and Petersen, S. (1997) Common blood flow changes across visual tasks: II. Decreases in cerebal cortex. *J. Cogn. Neurosci.*, **9**, 648 – 663.

[14] Biswal, B., Yetkin, F. Z., Haughton, V. M., and Hyde, J. S. (1995) Functional connectivity in the motor cortex of resting human brain using echo-planar MRI. *Magn Reson Med*, **34**, 537–41.

[15] Cordes, D., Haughton, V. M., Arfanakis, K., Carew, J. D., Turski, P. A., Moritz, C. H., Quigley, M. A., and Meyerand, M. E. (2001) Frequencies contributing to functional connectivity in the cerebral cortex in "resting-state" data. *AJNR Am J Neuroradiol*, **22**, 1326–33.

[16] Cordes, D., Haughton, V. M., Arfanakis, K., Wendt, G. J., Turski, P. A., Moritz, C. H., Quigley, M. A., and Meyerand, M. E. (2000) Mapping functionally related regions of brain with functional connectivity MR imaging. *AJNR Am J Neuroradiol*, **21**, 1636–44.

[17] De Luca, M., Smith, S., De Stefano, N., Federico, A., and Matthews, P. M. (2005) Blood oxygenation level dependent contrast resting state networks are relevant to functional activity in the neocortical sensorimotor system. *Exp Brain Res*, **167**, 587–94.

[18] Fox, M. D., Snyder, A. Z., Zacks, J. M., and Raichle, M. E. (2006) Coherent spontaneous activity accounts for trial-to-trial variability in human evoked brain responses. *Nat Neurosci*, **9**, 23–5.

[19] Lowe, M. J., Mock, B. J., and Sorenson, J. A. (1998) Functional connectivity in single and multislice echoplanar imaging using resting-state fluctuations. *Neuroimage*, **7**, 119–32.

[20] Xiong, J., Parsons, L. M., Gao, J. H., and Fox, P. T. (1999) Interregional connectivity to primary motor cortex revealed using MRI resting state images. *Hum Brain Mapp*, **8**, 151–6.

[21] Marder, E. and Weimann, J. (1991) *Neurobiology of motor program selection: new approaches to mechanisms of behavioral choice*. Manchester University Press.

[22] Bartels, A. and Zeki, S. (2005) The chronoarchitecture of the cerebral cortex. *Philos Trans R Soc Lond B Biol Sci*, **360**, 733–50.

[23] Beckmann, C. F., DeLuca, M., Devlin, J. T., and Smith, S. M. (2005) Investigations into resting-state connectivity using independent component analysis. *Philos Trans R Soc Lond B Biol Sci*, **360**, 1001–13.

[24] Damoiseaux, J. S., Rombouts, S. A., Barkhof, F., Scheltens, P., Stam, C. J., Smith, S. M., and Beckmann, C. F. (2006) Consistent resting-state networks across healthy subjects. *Proc Natl Acad Sci U S A*, **103**, 13848–53.

[25] De Luca, M., Beckmann, C. F., De Stefano, N., Matthews, P. M., and Smith, S. M. (2006) fMRI resting state networks define distinct modes of long-distance interactions in the human brain. *Neuroimage*, **29**, 1359–67.

[26] Greicius, M. D. and Menon, V. (2004) Default-mode activity during a passive sensory task: uncoupled from deactivation but impacting activation. *J Cogn Neurosci*, **16**, 1484–92.

[27] Kiviniemi, V., Kantola, J. H., Jauhiainen, J., Hyvärinen, A., and Tervonen, O. (2003) Independent component analysis of nondeterministic fMRI signal sources. *Neuroimage*, **19**, 253–60.

[28] Bell, A. J. and Sejnowski, T. J. (1995) An information-maximization approach to blind separation and blind deconvolution. *Neural Comput*, **7**, 1129–59.

[29] McKeown, M. J. and Sejnowski, T. J. (1998) Independent component analysis of fMRI data: examining the assumptions. *Hum Brain Mapp*, **6**, 368–72.

[30] Long, X. Y., et al. (2008) Default mode network as revealed with multiple methods for resting-state functional MRI analysis. *J Neurosci Methods*, **171**, 349–55.

[31] Raichle, M. E. (2010) Two views of brain function. *Trends Cogn Sci*, **14**, 180–90.

[32] Fox, M. D., Corbetta, M., Snyder, A. Z., Vincent, J. L., and Raichle, M. E. (2006) Spontaneous neuronal activity distinguishes human dorsal and ventral attention systems. *Proc Natl Acad Sci U S A*, **103**, 10046–51.

[33] Corbetta, M., Patel, G., and Shulman, G. L. (2008) The reorienting system of the human brain: from environment to theory of mind. *Neuron*, **58**, 306–24.

[34] Corbetta, M. and Shulman, G. L. (2002) Control of goal-directed and stimulus-driven attention in the brain. *Nat Rev Neurosci*, **3**, 201–15.

[35] Golland, Y., Bentin, S., Gelbard, H., Benjamini, Y., Heller, R., Nir, Y., Hasson, U., and Malach, R. (2007) Extrinsic and intrinsic systems in the posterior cortex of the human brain revealed during natural sensory stimulation. *Cereb Cortex*, **17**, 766–77.

[36] Hanson, S. J., Gagliardi, A. D., and Hanson, C. (2009) Solving the brain synchrony eigenvalue problem: conservation of temporal dynamics (fMRI) over subjects doing the same task. *J Comput Neurosci*, **27**, 103–14.

[37] Hasson, U., Furman, O., Clark, D., Dudai, Y., and Davachi, L. (2008) Enhanced intersubject correlations during movie viewing correlate with successful episodic encoding. *Neuron*, **57**, 452–62.

[38] Hasson, U., Landesman, O., Knappmeyer, B., Vallines, I., Rubin, N., and Heege, D. (2008) Neurocinematics: The neuroscience of film. *Projections*, **2**, 1 – 26.

[39] Hasson, U., Nir, Y., Levy, I., Fuhrmann, G., and Malach, R. (2004) Intersubject synchronization of cortical activity during natural vision. *Science*, **303**, 1634–40.

[40] Esposito, F., Seifritz, E., and Formisano, E. (2003) Real-time independent component analysis of fMRI time series. *Neuroimage*, **20**, 2209–2224.

[41] Ma, L., Wang, B., Chen, C., and Xiong, J. (2007) Detecting functional connectivity in the resting brain: a comparison between ICA and CCA. *Magn Reson Imaging*, **25**, 47–56.

[42] Green, C. and Cordes, D. (2002) Preprocessing funtional MRI data with principal component analysis adversely affects the results of independent component analysis. *Neuroimage*, **16(Suppl.)**, 357.

[43] Li, Y. O., Adali, T., and Calhoun, V. D. (2007) Estimating the number of independent components for functional magnetic resonance imaging data. *Hum Brain Mapp*, **28**, 1251–66.

[44] Huettel, S., Song, A., and McCarthy, G. (2004) *Functional Magnetic Resonance Imaging*. Sinauer Associates, 1 edn.

[45] Buxton, R. (2009) *Introduction to Functional Magnetic Resonance Imaging. Principles and Techniques.*. Cambridge University Press, 2 edn.

[46] Liang, Z. and Lauterbur, P. (2000) *Principles of magnetic resonance imaging. A signal processing perspective.*. IEEE Press in Biomedical Engineering.

[47] Ljunggren, S. (1983) A simple graphical representation of Fourier-based imaging methods. *J Magn Reson*, **54**, 338–343.

[48] Twieg, D. (1983) The k-trajectory formulation of the NMR imaging process with applications in analysis and synthesis of imaging methods. *Med Phys*, **10**, 610–621.

[49] Ogawa, S., Lee, T. M., Nayak, A. S., and Glynn, P. (1990) Oxygenation-sensitive contrast in magnetic resonance image of rodent brain at high magnetic fields. *Magn Reson Med*, **14**, 68–78.

[50] Mansfield, P. (1977) Multi-planar image formation using NMR spin echoes. *J Phys*, **C10**, L55–58.

[51] Aguirre, G. K., Zarahn, E., and D'Esposito, M. (1998) The variability of human, bold hemodynamic responses. *Neuroimage*, **8**, 360–9.

[52] Menon, R. S., Ogawa, S., Hu, X., Strupp, J. P., Anderson, P., and Ugurbil, K. (1995) BOLD based functional MRI at 4 Tesla includes a capillary bed contribution: echo-planar imaging correlates with previous optical imaging using intrinsic signals. *Magn Reson Med*, **33**, 453–9.

[53] Duong, T. Q., Kim, D. S., Ugurbil, K., and Kim, S. G. (2001) Localized cerebral blood flow response at submillimeter columnar resolution. *Proc Natl Acad Sci U S A*, **98**, 10904–9.

[54] Golland, Y., Golland, P., Bentin, S., and Malach, R. (2008) Data-driven clustering reveals a fundamental subdivision of the human cortex into two global systems. *Neuropsychologia*, **46**, 540–53.

[55] Hyvärinen, A. and Oja, E. (2000) Independent component analysis: algorithms and applications. *Neural Netw*, **13**, 411–30.

[56] Hyvärinen, A. (1999) Fast and robust fixed-point algorithms for independent component analysis. *IEEE Trans Neural Netw*, **10**, 626–34.

[57] Huber, P. (1985) Projection pursuit. *The Annals of Statistics*, **13**, 435–475.

[58] Cover, T. and Thomas, J. (1991) *Elements of Information Theory*. John Wiley & Sons.

[59] Jolliffe, I. (2002) *Principal component analysis*. Springer-Verlag, 2 edn.

[60] Rissanen, J. (1978) Modeling by the shortest data description. *Automatica*, **14**, 465–471.

[61] Himberg, J., Hyvärinen, A., and Esposito, F. (2004) Validating the independent components of neuroimaging time series via clustering and visualization. *Neuroimage*, **22**, 1214–22.

[62] Calhoun, V. D., Adali, T., Pearlson, G. D., and Pekar, J. J. (2001) A method for making group inferences from functional MRI data using independent component analysis. *Hum Brain Mapp*, **14**, 140–51.

[63] Duann, J., Jung, T., Makeig, S., and Sejnowski, T. (2003) Consistency of infomax ICA decomposition of functional brain imaging data. *In Proceedings of the fourth international workshop on independent component analysis and blind signal separation*, pp. 289–294.

[64] Ylipaavalniemi, J. and Vigário, R. (2008) Analyzing consistency of independent components: An fMRI illustration. *Neuroimage*, **39**, 169–180.

[65] Calhoun, V. D. and Adali, T. (2006) Unmixing fMRI with independent component analysis. *IEEE Eng Med Biol Mag*, **25**, 79–90.

[66] Koskela, M., Sjöberg, M., and Laaksonen, J. (2007) Rushes summarization with self-organizing maps. *TVS ACM MM'07*, Augsburg, Germany.

[67] Malinen, S. and Hari, R. (2010) Comprehension of audiovisual speech: Data-based sorting of independent components of fMRI activity. Tech. rep., Aalto University School of Science and Technology, Espoo.

[68] Yousry, T. A., Schmid, U. D., Alkadhi, H., Schmidt, D., Peraud, A., Buettner, A., and Winkler, P. (1997) Localization of the motor hand area to a knob on the precentral gyrus. A new landmark. *Brain*, **120 ( Pt 1)**, 141–57.

[69] Amiez, C., Kostopoulos, P., Champod, A. S., and Petrides, M. (2006) Local morphology predicts functional organization of the dorsal premotor region in the human brain. *J Neurosci*, **26**, 2724–31.

[70] Bray, S., Shimojo, S., and O'Doherty, J. P. (2007) Direct instrumental conditioning of neural activity using functional magnetic resonance imaging-derived reward feedback. *J Neurosci*, **27**, 7498–507.

[71] Davare, M., Lemon, R., and Olivier, E. (2008) Selective modulation of interactions between ventral premotor cortex and primary motor cortex during precision grasping in humans. *J Physiol*, **586**, 2735–42.

[72] Grefkes, C., Eickhoff, S. B., Nowak, D. A., Dafotakis, M., and Fink, G. R. (2008) Dynamic intra- and interhemispheric interactions during unilateral and bilateral hand movements assessed with fMRI and DCM. *Neuroimage*, **41**, 1382–94.

[73] Zhang, H., Zuo, X. N., Ma, S. Y., Zang, Y. F., Milham, M. P., and Zhu, C. Z. (2010) Subject order-independent group ICA (SOI-GICA) for functional MRI data analysis. *Neuroimage*, **51**, 1414–24.

[74] Jousmäki, V. and Hari, R. (1998) Parchment-skin illusion: sound-biased touch. *Curr Biol*, **8**, R190.

[75] Foxe, J. J., Wylie, G. R., Martinez, A., Schroeder, C. E., Javitt, D. C., Guilfoyle, D., Ritter, W., and Murray, M. M. (2002) Auditory-somatosensory multisensory processing in auditory association cortex: an fMRI study. *J Neurophysiol*, **88**, 540–3.

[76] Schürmann, M., Caetano, G., Jousmäki, V., and Hari, R. (2004) Hands help hearing: facilitatory audiotactile interaction at low sound-intensity levels. *J Acoust Soc Am*, **115**, 830–2.

[77] Schürmann, M., Caetano, G., Hlushchuk, Y., Jousmäki, V., and Hari, R. (2006) Touch activates human auditory cortex. *Neuroimage*, **30**, 1325–31.

[78] Erhardt, E. B., Rachakonda, S., Bedrick, E. J., Allen, E. A., Adali, T., and Calhoun, V. D. (2010) Comparison of multi-subject ICA methods for analysis of fMRI data. *Hum Brain Mapp*, **n/a**, Epub ahead of print, DOI: 10.1002/hbm.21170.

[79] Cordes, D. and Nandy, R. R. (2006) Estimation of the intrinsic dimensionality of fMRI data. *Neuroimage*, **29**, 145–54.

[80] Grezes, J. and Decety, J. (2001) Functional anatomy of execution, mental simulation, observation, and verb generation of actions: a meta-analysis. *Hum Brain Mapp*, **12**, 1–19.

[81] Lahnakoski, J. (2010) *Functional magnetic resonance imaging of human brain during rest and viewing movies*. Master's thesis, Aalto University School of Science and Technology, Espoo.

[82] Tomasi, D., Ernst, T., Caparelli, E. C., and Chang, L. (2006) Common deactivation patterns during working memory and visual attention tasks: an intra-subject fMRI study at 4 Tesla. *Hum Brain Mapp*, **27**, 694–705.